Atmos. Chem. Phys., 20, 4757–4785, 2020
https://doi.org/10.5194/acp-20-4757-2020

Atmospheric Chemistry and Physics
Open Access
EGU

Influx of African biomass burning aerosol during the Amazonian dry season through layered transatlantic transport of black carbon-rich smoke

Bruna A. Holanda[1,2,3], Mira L. Pöhlker[1], David Walter[1,4], Jorge Saturno[2,a], Matthias Sörgel[2,5], Jeannine Ditas[6,1], Florian Ditas[1,2,b], Christiane Schulz[7,8], Marco Aurélio Franco[3,1], Qiaoqiao Wang[6,2], Tobias Donth[9], Paulo Artaxo[3], Henrique M. J. Barbosa[3], Stephan Borrmann[8,10], Ramon Braga[1], Joel Brito[3,c], Yafang Cheng[1], Maximilian Dollner[11,12], Johannes W. Kaiser[5,d], Thomas Klimach[1], Christoph Knote[13], Ovid O. Krüger[1], Daniel Fütterer[12], Jošt V. Lavrič[4], Nan Ma[6,1], Luiz A. T. Machado[14,1], Jing Ming[1,2], Fernando G. Morais[3], Hauke Paulsen[1], Daniel Sauer[12], Hans Schlager[12], Johannes Schneider[8], Hang Su[1], Bernadett Weinzierl[11,12], Adrian Walser[11,12,13], Manfred Wendisch[9], Helmut Ziereis[12], Martin Zöger[15], Ulrich Pöschl[1], Meinrat O. Andreae[2,16], and Christopher Pöhlker[1,2]

[1]Multiphase Chemistry Department, Max Planck Institute for Chemistry, 55128 Mainz, Germany
[2]Biogeochemistry Department, Max Planck Institute for Chemistry, 55128 Mainz, Germany
[3]Instituto de Fisica, Universidade de Sao Paulo, 05508-090, Sao Paulo, SP, Brazil
[4]Max Planck Institute for Biogeochemistry, 07701 Jena, Germany
[5]Atmospheric Chemistry Department, Max Planck Institute for Chemistry, 55128 Mainz, Germany
[6]Institute for Environmental and Climate Research (ECI), Jinan University, Guangzhou, 511443, China
[7]Experimental Aerosol and Cloud Microphysics Department, TROPOS, Leibniz-Institute for Tropospheric Research, Leipzig, Germany
[8]Particle Chemistry Department, Max Planck Institute for Chemistry, 55128 Mainz, Germany
[9]Leipzig Institute for Meteorology, Leipzig University, Leipzig, Germany
[10]Institute for Physics of the Atmosphere, Johannes Gutenberg University, 55128 Mainz, Germany
[11]University of Vienna, Faculty of Physics, Aerosol Physics and Environmental Physics, 1090 Vienna, Austria
[12]Institute for Atmospheric Physics, German Aerospace Center (DLR), 82234 Oberpfaffenhofen, Germany
[13]Meteorological Institute, Ludwig-Maximilians-Universität, Munich, Germany
[14]National Institute for Space Research (INPE), São José Dos Campos, Brazil
[15]Flight experiments, German Aerospace Center (DLR), 82234 Oberpfaffenhofen, Germany
[16]Scripps Institution of Oceanography, University of California San Diego, La Jolla, California 92093, USA
[a]now at: Physikalisch-Technische Bundesanstalt, 38116 Braunschweig, Germany
[b]now at: Hessisches Landesamt für Naturschutz, Umwelt und Geologie, 65203 Wiesbaden, Germany
[c]now at: IMT Lille Douai, Univ. Lille, SAGE, 59000 Lille, France
[d]now at: Deutscher Wetterdienst, 63067 Offenbach, Germany

Correspondence: Mira L. Pöhlker (m.pohlker@mpic.de) and Christopher Pöhlker (c.pohlker@mpic.de)

Received: 29 August 2019 – Discussion started: 2 September 2019
Revised: 6 January 2020 – Accepted: 4 March 2020 – Published: 24 April 2020

Published by Copernicus Publications on behalf of the European Geosciences Union.

Abstract. Black carbon (BC) aerosols influence the Earth's atmosphere and climate, but their microphysical properties, spatiotemporal distribution, and long-range transport are not well constrained. This study presents airborne observations of the transatlantic transport of BC-rich African biomass burning (BB) smoke into the Amazon Basin using a Single Particle Soot Photometer (SP2) as well as several complementary techniques. We base our results on observations of aerosols and trace gases off the Brazilian coast onboard the HALO (High Altitude and LOng range) research aircraft during the ACRIDICON-CHUVA campaign in September 2014.

During flight AC19 over land and ocean at the northeastern coastline of the Amazon Basin, we observed a BC-rich layer at ~ 3.5 km altitude with a vertical extension of ~ 0.3 km. Backward trajectories suggest that fires in African grasslands, savannas, and shrublands were the main source of this pollution layer and that the observed BB smoke had undergone more than 10 d of atmospheric transport and aging over the South Atlantic before reaching the Amazon Basin. The aged smoke is characterized by a dominant accumulation mode, centered at about 130 nm, with a particle concentration of $N_{acc} = 850 \pm 330\,cm^{-3}$. The rBC particles account for $\sim 15\,\%$ of the submicrometer aerosol mass and $\sim 40\,\%$ of the total aerosol number concentration. This corresponds to a mass concentration range from 0.5 to $2\,\mu g\,m^{-3}$ (1st to 99th percentiles) and a number concentration range from 90 to $530\,cm^{-3}$. Along with rBC, high c_{CO} (150 ± 30 ppb) and c_{O_3} (56 ± 9 ppb) mixing ratios support the biomass burning origin and pronounced photochemical aging of this layer. Upon reaching the Amazon Basin, it started to broaden and to subside, due to convective mixing and entrainment of the BB aerosol into the boundary layer. Satellite observations show that the transatlantic transport of pollution layers is a frequently occurring process, seasonally peaking in August/September.

By analyzing the aircraft observations together with the long-term data from the Amazon Tall Tower Observatory (ATTO), we found that the transatlantic transport of African BB smoke layers has a strong impact on the northern and central Amazonian aerosol population during the BB-influenced season (July to December). In fact, the early BB season (July to September) in this part of the Amazon appears to be dominated by African smoke, whereas the later BB season (October to December) appears to be dominated by South American fires. This dichotomy is reflected in pronounced changes in aerosol optical properties such as the single scattering albedo (increasing from 0.85 in August to 0.90 in November) and the BC-to-CO enhancement ratio (decreasing from 11 to $6\,ng\,m^{-3}\,ppb^{-1}$). Our results suggest that, despite the high fraction of BC particles, the African BB aerosol acts as efficient cloud condensation nuclei (CCN), with potentially important implications for aerosol–cloud interactions and the hydrological cycle in the Amazon.

1 Introduction

Biomass burning (BB) in the African and South American tropics and subtropics represents a globally significant source of atmospheric aerosol particles and trace gases (Andreae, 1991; Andreae et al., 1988; Barbosa et al., 1999; Ichoku and Ellison, 2014; Kaiser et al., 2012; Reddington et al., 2016; van der Werf et al., 2017). A major constituent of BB smoke is black carbon (BC), which is co-emitted along with organic aerosols and inorganic salts in proportions that depend on the fuel type and fire phase (Allen and Miguel, 1995; Andreae, 2019; Andreae and Merlet, 2001; Jen et al., 2019; Levin et al., 2010; Reid et al., 2005). The BC aerosol is a key component in the climate system as it significantly influences the Earth's radiative budget through the so-called direct, semi-direct, and indirect aerosol effects (Bond et al., 2013; Boucher et al., 2016; Brioude et al., 2009; Koch and Del Genio, 2010; IPCC, 2013). Recent studies have classified BC as the second largest contributor to global warming and estimated its direct radiative forcing to be as high as $+1.1\,W\,m^{-2}$, with 90 % uncertainty bounds spanning from $+0.17$ to $+2.1\,W\,m^{-2}$ (Bond et al., 2013, and references therein). This large uncertainty arises from our poor understanding of the BC microphysical properties and its spatiotemporal distribution in the atmosphere (Boucher et al., 2013; Andreae and Ramanathan, 2013). During their typical atmospheric lifetime of several days, BC particles undergo photochemical aging, creating internally mixed BC aerosols via the condensation of low and semi-volatile compounds, coagulation, and cloud processing (Bond et al., 2013; Cubison et al., 2011; Konovalov et al., 2017, 2019; Schwarz et al., 2008; Willis et al., 2016). The formation of non-absorbing or semi-transparent coatings on the BC cores changes the particles' optical properties (Fuller et al., 1999; Moffet and Prather, 2009; Pokhrel et al., 2017; Schnaiter, 2005; Zhang et al., 2015) as well as their ability to act as cloud condensation nuclei (CCN) (Laborde et al., 2013; Liu et al., 2017; Tritscher et al., 2011), which influences their atmospheric transport and lifetime.

The Amazonian atmosphere is strongly influenced by the yearly north–south oscillation of the Intertropical Convergence Zone (ITCZ) (Andreae et al., 2012; Martin et al., 2010; Pöhlker et al., 2019), which causes a pronounced seasonality in aerosol concentrations (e.g., BC and CCN) and other aerosol properties (e.g., single scattering albedo) (Roberts et al., 2001; Roberts, 2003; Martin et al., 2010; Artaxo et al., 2013; Rizzo et al., 2013; Andreae et al., 2015; Pöhlker et al., 2016; Saturno et al., 2018b). This makes the central Amazon Basin an ideal environment to study atmospheric and biogeochemical processes as a function of the highly variable aerosol population. During the wet season (February to May), trace gas and aerosol emissions from the regional biosphere predominantly regulate atmospheric cycling, precipitation patterns, and regional climate (Pöhlker et al., 2012; Pöschl et al., 2010). Average wet season black carbon (BC)

mass concentrations, M_{BC}, are $\sim 0.07\,\mu g\,m^{-3}$, and M_{BC} approaches zero during pristine episodes (Andreae and Gelencsér, 2006; Pöhlker et al., 2018). In contrast, the dry season (August to November) is characterized by intense and persistent BB emissions, changing substantially the atmospheric composition and cycling (Artaxo et al., 2013; Rizzo et al., 2013). Average dry season BC mass concentrations (M_{BC}) in central Amazonia are $\sim 0.4\,\mu g\,m^{-3}$, with peaks reaching $\sim 0.9\,\mu g\,m^{-3}$ (Pöhlker et al., 2018; Saturno et al., 2018b), while in the southern hotspot regions of agriculture-related burning, the average M_{BC} can be as high as $\sim 2.8\,\mu g\,m^{-3}$ (Artaxo et al., 2013).

Several studies have found that the long-range transport (LRT) of long-lived species from Africa plays a major role in the Amazonian atmospheric composition. The transport of dust from distant sources into the heart of the Amazon Basin was first observed in 1977, although Africa was not identified as the source region at the time (Lawson and Winchester, 1979). Subsequently, the plume-wise LRT of African dust and smoke during the Amazonian wet season has been well documented (Ansmann et al., 2009; Baars et al., 2011; Barkley et al., 2019; Moran-Zuloaga et al., 2018; Swap et al., 1992; Talbot et al., 1990; Wang et al., 2016). The LRT of aerosols occurs also during the Amazonian dry season, when smoke from the intense African BB plays a substantial role. The earliest observations of such pollution layers in the free troposphere over the Brazilian coast can be found in ozone (O_3) soundings made from Natal, on the eastern coast of Brazil (5.8° S, 35.2° W), where mixing ratios of ~ 70 ppb were measured with a maximum in the month of September (Kirchhoff et al., 1983; Logan and Kirchhoff, 1986). These measurements were continued over a 10-year period (1978–1988), confirming the climatological presence of a tropospheric O_3 maximum over the Brazilian coast, centered at the 500 hPa pressure level and peaking in the September–October period (Kirchhoff et al., 1991).

The first comprehensive airborne measurements off the South American coast, made in 1989 near Natal, could also attribute these pollution layers to LRT of African BB emissions (Andreae et al., 1994). Additional aircraft campaigns in southern Africa, the tropical South Atlantic, and the Amazon Basin have found pollution layers in the free troposphere with similar characteristics (e.g., Andreae et al., 1988; Diab et al., 1996; Thompson et al., 1996; Bozem et al., 2014; Marenco et al., 2016). Recent studies in the central basin, at the Amazon Tall Tower Observatory (ATTO) and at the northeastern edge of the Amazon, found indications of a significant abundance of African smoke during the Amazonian dry season (Barkley et al., 2019; Pöhlker et al., 2019, 2018; Saturno et al., 2018b; Wang et al., 2016). However, robust quantitative data from observations and/or models (e.g., African BC and CCN fractions in the Amazon Basin) have remained sparse.

This study focusses on the transatlantic transport of African BB smoke into the Amazon Basin by combining in situ aircraft observations, modeling results, and remote sensing data. The core of this work is aircraft observations made within a defined African pollution layer upon its arrival at the South American coast during the ACRIDICON-CHUVA campaign over Amazonia in September 2014 (Wendisch et al., 2016). We focus primarily on the spatiotemporal distribution and advection dynamics of the BB smoke layers by analyzing (i) aerosol and trace gas concentration profiles, (ii) backward trajectories and African BB source regions, (iii) the seasonality of the pollution transport, (iv) the horizontal and vertical extents of the transported layers, and (v) the convective mixing and smoke entrainment from the layers into the planetary boundary layer as they are transported from the ocean into the South American continent. Note that a detailed characterization of the microphysical aerosol properties within the BB smoke layers (e.g., the BC core diameters and mixing state) is beyond the scope of the present work and will be the subject of a separate follow-up study. As a final step of the present study, we integrate its main results into the broader picture of the long-term aerosol observations at the central Amazonian ATTO site to estimate the relevance of African pollution for the aerosol lifecycle in the dry season.

2 Materials and methods

2.1 The ACRIDICON-CHUVA campaign

The data presented here were obtained during flight AC19 of the ACRIDICON-CHUVA aircraft campaign (Machado et al., 2018; Wendisch et al., 2016), which took place over the Atlantic Ocean and the Amazon Basin on 30 September 2014. The main objective of ACRIDICON-CHUVA was to study the interactions between aerosol particles, deep convective clouds, and atmospheric radiation using a broad set of instruments for airborne observations of aerosol physical and chemical properties, trace gases, radiation, and cloud. The measurements were conducted onboard the German HALO (High Altitude and LOng range) research aircraft, operated by the German Aerospace Center (DLR), covering a wide geographic area of the Amazon Basin and probing different pollution states by means of highly resolved atmospheric profiles (altitudes up to 15 km).

2.2 Airborne measurements of aerosol, trace gas, and meteorology during ACRIDICON-CHUVA

Navigation and basic meteorological data (e.g., air pressure, temperature, humidity, and water vapor mixing ratio) were obtained from the BAsic HALO Measurement And Sensor System (BAHAMAS) at 1 s time resolution. BAHAMAS acquires data from air flow and thermodynamic sensors as well as from the aircraft avionics and a high-precision inertial reference system to derive basic meteorological parameters like pressure, temperature, and the 3-D wind vector,

as well as aircraft position and attitude. Water vapor mixing ratio and further derived humidity parameters are measured by SHARC (Sophisticated Hygrometer for Atmospheric ResearCh) based on direct absorption measurement by a tunable diode laser (TDL) system. Typical absolute accuracy of the basic meteorological data is 0.5 K for temperature, 0.3 hPa for pressure, 0.4–0.6 m s^{-1} for wind, and 5 % (+1 ppm) for water vapor mixing ratio. All aerosol concentration data were normalized to standard temperature and pressure (STP, $T_0 = 273.15$ K, $p_0 = 1013.25$ hPa). Most of the aerosol sampling was conducted through the HALO aerosol submicrometer inlet (HASI), which provides up to 30 L min^{-1} sample air flow divided over four sample lines. The air stream sampled on top of the fuselage is aligned with the inlet using a front shroud and decelerated by a factor of approximately 15, providing near-isokinetic sampling to the aerosol instruments mounted inside the aircraft cabin (Andreae et al., 2018).

The characterization of refractory black carbon (rBC) particles at high time resolution was conducted using an eight-channel Single Particle Soot Photometer (SP2, Droplet Measurement Techniques, Longmont, CO, USA) (Stephens et al., 2003; Schwarz et al., 2006). The instrument measures the time-dependent scattering and incandescence signals produced by single aerosol particles when crossing a Gaussian-shaped laser beam (Nd:YAG; wavelength $\lambda = 1064$ nm) (Schwarz et al., 2006). The avalanche photo-diode (APD) detectors measure at high and low gain stages the aerosol particle light scattering and incandescence in two wavelength ranges ($\lambda = 350$–800 nm and $\lambda = 630$–880 nm). All particles scatter the laser light with an intensity that is proportional to their optical size, from which the optical diameter (D_o) is determined. The instrument detects purely scattering particles in the size range of 200 nm $< D_o <$ 400 nm. Particles containing sufficient mass of rBC absorb the laser light and are heated to their vaporization temperature (~ 4000 °C), emitting incandescence light. The peak intensity of the incandescence signal is linearly proportional to the mass of rBC in the particle, which is determined after applying a calibration factor (Laborde et al., 2013). Assuming a void-free density of 1.8 g cm^{-3}, the mass-equivalent diameter (D_{MEV}) of rBC cores is calculated from the measured rBC mass (Laborde et al., 2013). The SP2 measurements are sensitive to rBC cores in the nominal size range of 70 nm $< D_{MEV} <$ 500 nm. The SP2 incandescence signal was calibrated at the beginning, during, and at the end of the campaign, using size-selected fullerene soot particles. The scattering signal was calibrated using spherical polystyrene latex spheres (208, 244, and 288 nm) and ammonium sulfate particles with diameters selected by a differential mobility analyzer (DMA, Grimm Aerosol Technik, Ainring, Germany). The results of all calibrations agreed within their uncertainty ranges, confirming good instrument stability throughout the campaign.

The concentration of condensation nuclei, N_{CN}, was measured using a butanol-based condensation particle counter (CPC, Grimm Aerosol Technik) with a nominal lower cutoff particle diameter of 4 nm. Due to losses in the inlet lines, the effective cutoff diameter was ~ 10 nm at lower atmospheric levels and ~ 20 nm in the upper troposphere. Accordingly, total aerosol concentrations will be represented by $N_{CN,20}$. An additional CPC with the same cutoff diameter was connected to a thermodenuder, which heats a segment of the sample line to 250 °C. The thermodenuder is used to evaporate the volatile aerosol constituents, such as organics and ammonium sulfate salts, allowing one to quantify the non-volatile (or refractory) particles (e.g., mineral dust, black carbon, sea salt) (Clarke, 1991; Weinzierl et al., 2011). In addition, the particle number size distributions (PNSD) of aerosols in the size range of $D_p = 90$–600 nm were obtained from an Ultra-High Sensitivity Aerosol Spectrometer (UHSAS; Droplet Measurement Technologies, Longmont, CO, USA) (Cai et al., 2008). In this paper, we refer to the total number concentration measured by the UHSAS as the accumulation-mode number concentration, N_{acc}. The ultrafine fraction (f_{fine}) is obtained as the difference between the CPC particle counts, $N_{CN,20}$, and the N_{acc} obtained by the UHSAS, divided by $N_{CN,20}$. Likewise, the volatile fraction (f_{vol}) is obtained from the difference between aerosol counts measured by the two CPCs (with and without a thermodenuder) divided by $N_{CN,20}$.

The CCN concentration, N_{CCN}, was measured with a two-column CCN counter (CCNC, model CCN-200, DMT, Longmont, CO, USA) (Krüger et al., 2014; Roberts and Nenes, 2005; Rose et al., 2008). In this study, we used only the measurements at constant supersaturation ($S = 0.52 \pm 0.05$ %). The activated fraction, $f_{CCN,0.5}$, was calculated as $N_{CCN,0.5}$ divided by $N_{CN,20}$.

A compact time-of-flight aerosol mass spectrometer (C-ToF-AMS, Aerodyne Research, Inc., Billerica, MA, USA) measured the mass concentration of four chemical species (i.e., organics, sulfate, nitrate, and ammonium) of the submicrometer aerosol with a time resolution of 30 s (Drewnick et al., 2005; Schulz et al., 2018). A complete description of the instrument and its operation during the ACRIDICON-CHUVA campaign is given in Schulz et al. (2018) and Andreae et al. (2018).

A dual-cell ultraviolet (UV) absorption detector (TE49C, Thermo Scientific) operating at a wavelength of $\lambda = 254$ nm was used to measure O_3 with a precision of 2 % or 1 ppb. The CO mixing ratio was detected with a fast-response fluorescence instrument (AL5002, Aerolaser, Garmisch, Germany) (Gerbig et al., 1999). NO and total reactive nitrogen, NO_y, were measured by a modified dual-channel chemiluminescence detector (CLD-SR, Ecophysics) in connection with a gold converter (Baehr, 2003; Ziereis et al., 2000). More details on the measurement techniques can be found in Andreae et al. (2018).

The rBC enhancement ratio relative to CO ($EnR_{BC,M} = \Delta M_{rBC}/\Delta c_{CO}$, where Δ is the difference between the concentration of the species in the plume and in the background atmosphere) was obtained by applying a bivariate fit

to the rBC and CO correlation within individual pollution plumes. Analogously, CCN and rBC enhancement ratios relative to total CPC particle counts ($\Delta N_{CCN,0.5}/\Delta N_{CN,20}$ and $\Delta N_{rBC}/\Delta N_{CN,20}$) were obtained by applying a bivariate fit between the respective quantities. Note that the best fit for the c_{CO} vs. M_{rBC} correlation was obtained after multiplying the c_{CO} by a factor such that their means are numerically equivalent and then multiplying the resulting fit parameter by the same factor to obtain the $EnR_{BC,M}$.

2.3 Ground-based aerosol and trace gas measurements at ATTO

The ATTO site was established in 2010/2011 as a research platform for in-depth and long-term measurements of aerosol particles and trace gases as well as meteorological and ecological parameters in the central Amazon rain forest (Andreae et al., 2015). The research site is located 150 km northeast of Manaus, in a region characterized by periodic pristine atmospheric conditions during parts of the wet season vs. strong BB pollution during the dry season (Pöhlker et al., 2016, 2018; Saturno et al., 2018b). The present study includes ATTO data of the aerosol absorption coefficient at $\lambda = 637$ nm, σ_{ap}, using the Multiangle Absorption Photometer (MAAP, model 5012, Thermo Electron Group, Waltham, USA) and the aerosol scattering coefficients, σ_{sp}, using a nephelometer (model Aurora 3000, Ecotech Pty Ltd., Knoxfield, Australia), respectively. The M_{BC_e} was calculated using a mass absorption cross section of $12.3\,m^2\,g^{-1}$ for the dry season, as obtained by Saturno et al. (2018b). The single scattering albedo (SSA), which characterizes the absorption properties of an aerosol population, is defined as scattering divided by total extinction (absorption + scattering). All data were normalized to standard temperature and pressure (STP, $T_0 = 273.15$ K, $p_0 = 1013.25$ hPa). The CCN concentrations at a supersaturation of 0.5 %, $N_{CCN,0.5}$, were calculated using long-term scanning mobility particle sizer (SMPS) data and the κ-Köhler parametrization as described in Pöhlker et al. (2016). For more details about the aerosol optical properties' characterization and CCN observations, we refer the reader to Saturno et al. (2018b) and Pöhlker et al. (2016, 2018), respectively. Further details on CO measurements conducted at the ATTO site can be found in Winderlich et al. (2010) and Andreae et al. (2015). Daily EnR_{BC} was calculated by applying a bivariate regression fit to 30 min averages of ΔBC_e and ΔCO. The 5th percentiles of the BC_e and CO measurements of the corresponding month were used as background values.

2.4 Satellite and ground-based remote sensing

In this study, we used the vertically resolved extinction coefficients (LIDAR Level 2 Version 3 Aerosol Profile product with 5 km horizontal resolution) of the Cloud-Aerosol Lidar with Orthogonal Polarization (CALIOP) lidar system, onboard the Cloud-Aerosol Lidar and Infrared Pathfinder Satellite Observations (CALIPSO) satellite (Winker et al., 2009). The CALIPSO algorithms detect and classify aerosol layers based on their observed physical and optical properties into the subclasses polluted continental, biomass burning (smoke), desert dust, polluted dust, clean continental, and marine aerosol (Omar et al., 2009).

To obtain CO concentrations between the 400 and 600 hPa pressure levels, we used the Atmospheric Infrared Sounder (AIRS) onboard the NASA Aqua satellite available from the Giovanni online data system (https://giovanni.gsfc.nasa.gov/giovanni/, last access: 13 June 2019). Daily averages of aerosol optical depth (AOD) at 550 nm with an original grid resolution of $1^\circ \times 1^\circ$ were obtained from Moderate Resolution Imaging Spectroradiometer (MODIS) aerosol products from the NASA Terra and Aqua satellites (Remer et al., 2005). Finally, AOD at 500 nm (level 2.0) was obtained by direct sun measurements in Ascension Island (7.976° S, 14.415° W), using the CIMEL sunphotometer of the AErosol RObotic NETwork (AERONET, https://aeronet.gsfc.nasa.gov/, last access: 12 March 2019) (Holben et al., 1998).

2.5 Direct radiative forcing at the top of the atmosphere

In this study, we used the library for radiative transfer (LibRadtran) (Emde et al., 2016) with the uvspec tool to calculate the direct radiative forcing at the top of the atmosphere (DRF-TOA) by aerosol particles in the BB layer in the region of the South Atlantic Ocean. To solve the radiative transfer equation, we chose the Discrete Ordinate Radiative Transfer solver (DISORT) 2 (Evans, 1998; Stamnes et al., 2000). The setup for the atmosphere was based on the standard tropical profile (Anderson et al., 1986), which was modified with measurement data. The vertical profiles of the mean aerosol extinction coefficient were calculated based on multi-year (2012–2018) CALIPSO retrievals. The extraterrestrial spectrum was used as described in Gueymard (2004). A wavelength range from 300 to 4000 nm was considered. The ocean was set as the underlying surface. The AOD of the plume was calculated by integrating the mean extinction coefficient over the altitude band of the pollution layer (1–5 km). A SSA of 0.84 was assumed for the smoke layer based on Zuidema et al. (2016) and Sect. 3.5 of the present study. An asymmetry parameter of 0.7 was used based on the typical BC value presented in Cheng et al. (2014). With the above parametrization, we obtained the mean daily value for the DRF-TOA along different longitudes.

2.6 Backward trajectory modeling and fire intensities

The HYbrid Single-Particle Lagrangian Integrated Trajectory (HYSPLIT) model (Stein et al., 2015) was used to obtain systematic and multi-year sets of backward trajectories

(BTs) for the ATTO site as outlined in detail in Pöhlker et al. (2019). The time series of cumulative fire intensity along the BTs (CF_{BT}) was calculated based on (i) an ensemble of filtered 3 d HYSPLIT BTs, started every hour in the time frame between 1 January 2013 and 31 December 2018, at a starting height of 200 m, and (ii) daily georeferenced fire intensity maps, in W m^{-2}, from the Global Fire Assimilation System (GFAS). The GFAS fire intensity maps were obtained as NetCDF3 files with a spatial resolution of 0.1° latitude by 0.1° longitude (0.1° equals roughly 11 km). Only those segments of the individual BTs in convective exchange with the surface/fires (i.e., BT segments with heights < 1000 m) and encountering *en route* convection (i.e., BT segments with sun fluxes > 50 W m^{-2}) were included in the calculation of CF_{BT}. In addition, the individual BTs were terminated upon *en route* occurrence of rain (i.e., for rainfall > 2 mm). Details of the BT data set and filtering can be found in Pöhlker et al. (2019).

We calculated the cumulative fire intensity for each trajectory as follows: every two consecutive points of the original trajectory (1 h time step) build one linear segment of a trajectory with length (L_i) $1 < i < 72$ h (see Fig. S1 in the Supplement). For each trajectory segment, the collection of grid cells (m, n) that the trajectory passes through is computed: this is done by finding all locations along the trajectory for which either the latitude or longitude coordinate is an integer multiplied by 0.1°. To account for the residence time of air mass at each grid cell, the length ($l_{i,j}$) of the trajectory path within the cell (m, n) is calculated, divided by the length of the trajectory segment (L_i) and multiplied by the fire intensity ($F_{m,n}$) corresponding to the grid cell (m, n). This results in the fire intensity weighted by the residence time of the air parcel along the segment. The cumulative fire intensity (cumFire) along every individual BT is calculated by summing up $F_{m,n}$ over the whole trajectory length. Note that as we used 3 d BTs, each trajectory was mapped to the raster of fire intensities of the 3 corresponding days (see the example in Fig. S2). Finally, we summed up the cumulative fire intensities over the 24 BTs for each day in order to obtain the CF_{BT} time series with 1 d time resolution.

The method described above is summarized in the following equations. Let F be a matrix containing fire intensities of size $M \times N$. Let T be a list of K trajectories.

$$\text{cumFire} = \sum_{j} \sum_{i=1}^{72} F_{m,n} \cdot \frac{l_{i,j}}{L_i}, \tag{1}$$

and $l_{i,j}$ is the path of trajectory segment within cell $F_{m,n}$, calculated as follows:

$$l_{i,j} = \sqrt{\left((x_{m+1} - x_m) \cdot \cos\left(\frac{y_{n+1} + y_n}{2}\right)\right)^2 + (y_{n+1} - y_n)^2}. \tag{2}$$

Finally, for the ensemble of 24 trajectories at each day,

$$\text{CF}_{\text{BT}} = \sum_{k=0}^{24} \text{cumFire}(T_k). \tag{3}$$

2.7 GIS data products and analysis

The analysis of geographic information system (GIS) data sets was conducted with the QGIS software package (Las Palmas version 2.18.2, QGIS development team). The GIS data sets were handled using the coordinate reference of the World Geodetic System from 1984 (WGS84). The following GIS data sets were used in this study: (i) maps of global water bodies obtained from the European Space Agency (ESA) (https://www.esa-landcover-cci.org/?q=node/162, last access: 4 July 2019), (ii) wind fields from the Modern-Era Retrospective analysis for Research and Applications Version 2 model (Merra-2, https://gmao.gsfc.nasa.gov/reanalysis/MERRA-2/, last access: 4 July 2019) obtained through the Giovanni online data system, (iii) land cover maps obtained from ESA (http://maps.elie.ucl.ac.be/CCI/viewer/index.php, last access: 4 July 2019), and (iv) a map of global biomes according to Olson et al. (2001). For further details, we refer the reader to Pöhlker et al. (2019).

3 Results and discussion

The flight track of AC19 followed the direction of the Amazon River from Manaus towards the coast and included cloud-profiling maneuvers over the Atlantic Ocean (Fig. 1). A remarkable observation during AC19 was the strong stratification of the troposphere over the ocean with vertically well-defined and horizontally extended layers, with varying degrees of pollution. Based on contrasting aerosol concentrations, size ranges, and composition, we distinguished an upper and a lower pollution layer (UPL and LPL) with a horizontal clean air mass layer (CL) in between. The layers were discernible visually from the aircraft cockpit (Fig. 2).

In this study, we present the tropospheric stratification for the lowest 5 km of the atmosphere, focusing primarily on aerosol and trace gas properties within the UPL, and contrast them with the properties of the CL, LPL, and marine boundary layer (MBL). Aerosol properties in the upper troposphere during ACRIDICON-CHUVA have been characterized in previous studies (Andreae et al., 2018; Schulz et al., 2018). Upon ascent and descent, the UPL was probed six times at offshore locations[1], right before it reached the South American continent, and two times onshore ∼200–400 km from the coastline (blue squares in Fig. 1). The eight UPL penetrations were several hundred kilometers apart from each other, underlining the large horizontal extent of the layer. Later on the route back to Manaus airport, we observed an active fire

[1]Note that we count the two passages through the layer over the Amazon River delta as offshore.

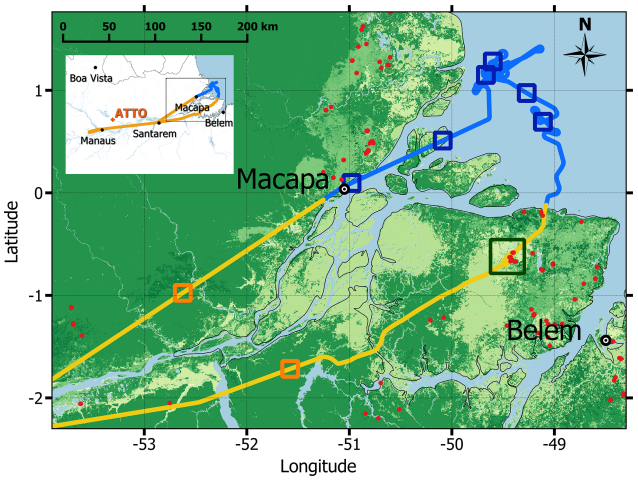

Figure 1. ACRIDICON-CHUVA flight AC19 on 30 September 2014. The squares represent the locations at which the aircraft ascended or descended through the upper pollution layer (UPL) (blue: offshore profiles, orange: inshore profiles). The yellow and blue segments of the flight track correspond to the inshore and offshore sections that were averaged to obtain the profiles in Fig. 3. Red markers indicate fire spots on 30 September 2014 as obtained from INPE (http://www.inpe.br/queimadas/bdqueimadas/, last access: 17 April 2019), and the dark green square represents the location where a fresh BB plume was probed at $\sim$ 1 km altitude.

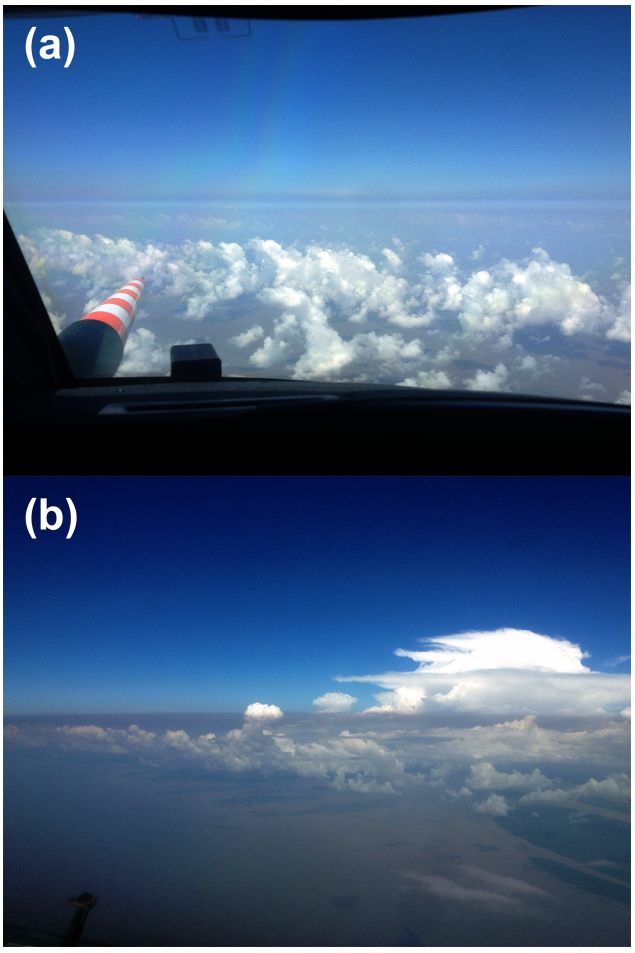

Figure 2. View from the HALO cockpit during flight AC19 on 30 September 2014, showing **(a)** the layering of the troposphere with clearly visible pollution layers as well as a clean layer in between at an offshore location (17:09 UTC) and **(b)** the brownish pollution layer arriving at the Brazilian coastline (16:55 UTC).

plume northwest of Belém (green square in Fig. 1, photo of plume in Fig. S3). This plume was probed at $\sim$ 1 km above the fire and is expected to be only a few minutes old. Selected aerosol properties at this local, fresh BB plume are contrasted with the UPL aerosol properties.

3.1 Offshore aerosol particle and trace gas profiles

The pronounced tropospheric stratification observed over the Atlantic Ocean near the northeastern margin of the Amazon Basin is illustrated by selected meteorological, trace gas, and aerosol profiles in Fig. 3. In Fig. 3a, the profiles of water vapor mass mixing ratio, q, and potential temperature, θ, show rather small interquartile ranges, indicating comparable q and θ conditions where profiling maneuvers were conducted along the flight track. In relation to q and θ, a well-defined layering – particularly the UPL – clearly emerges in the aerosol particle and trace gas properties (Fig. 3, Table 1). Generally, the profile of θ indicates rather stable conditions along the entire profile, with the UPL being centered at $\sim$ 3.5 km altitude. For comparison, radiosonde profiles at Belém airport for the same day as flight AC19 are shown in Fig. S4. The stable conditions presumably prevented the pollution from being mixed downwards and further suggest that the UPL is decoupled from the air masses above and below, facilitating an efficient horizontal transport pathway for the pollutants. Moreover, the distinct properties of the UPL, CL, and LPL as outlined below suggest that the corresponding air masses originated from different sources and/or processes and probably reflect different atmospheric aging times (see also Sect. 3.2). For example, shallow convection (or Scu) can increase aerosol at the top of clouds through detrainment.

In terms of aerosol properties, the UPL is characterized by a relative maximum in total number concentrations, $N_{CN,20} = 970 \pm 260\,cm^{-3}$ (mean $\pm$ 1 SD, Fig. 3b). Aerosol particles in the accumulation mode dominate the UPL aerosol, as $N_{acc} = 850 \pm 330\,cm^{-3}$ accounts for most of $N_{CN,20}$ ($\sim$ 85 %). This corresponds to a significant drop in the ultrafine particle fraction with $f_{fine} \approx 15$ % within the UPL (Fig. 3b). The aerosols in the UPL are further characterized by a low fraction of volatile particles, f_{vol}, as shown in Fig. 3c. In the atmospheric column, f_{vol} reaches its minimum of 16 ± 9 % within the UPL and generally shows a similar profile to f_{fine}, indicating a rather aged plume (Grieshop et al., 2009; Zhou et al., 2017). The particle number size distributions of the UPL aerosol – in comparison

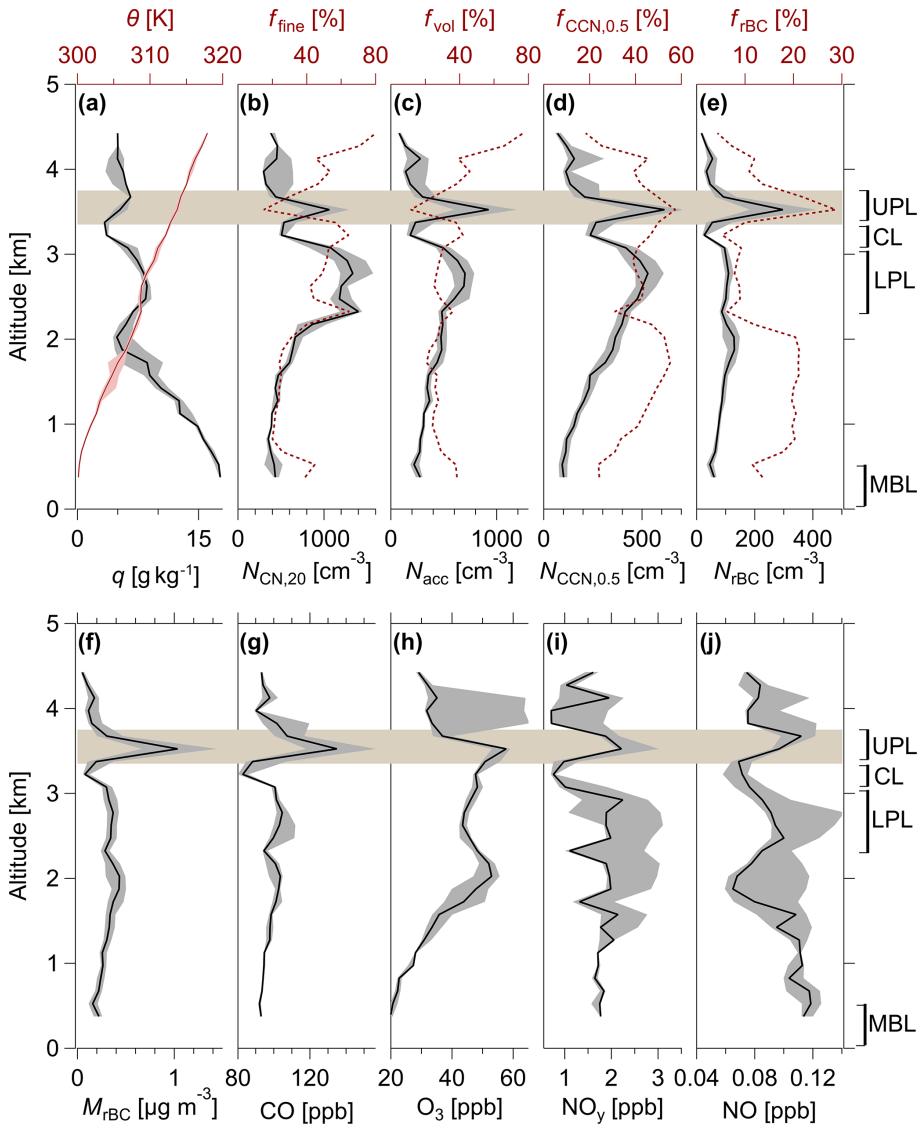

Figure 3. Vertical profiles of selected meteorological, aerosol, and trace gas parameters measured off the Brazilian coast during flight AC19: **(a)** potential temperature, θ, and water vapor mass mixing ratio, q; **(b)** total aerosol particle number concentration, $N_{\mathrm{CN},20}$, and ultrafine particle number fraction, f_{fine}; **(c)** accumulation-mode particle number concentration, N_{acc}, and volatile particle number fraction, f_{vol}; **(d)** CCN number concentration at $S = 0.5\,\%$, $N_{\mathrm{CCN},0.5}$, and activated fraction at $S = 0.5\,\%$, $f_{\mathrm{CCN},0.5}$; **(e)** rBC number concentration, N_{rBC}, and rBC number fraction, $f_{\mathrm{rBC},N}$; and **(f)** rBC mass concentration, M_{rBC}; **(g)** carbon monoxide, c_{CO}; **(h)** ozone, $c_{\mathrm{O_3}}$; **(i)** total reactive nitrogen, $c_{\mathrm{NO_y}}$; and **(j)** nitrogen monoxide, c_{NO}, mole fractions measured off the Brazilian coast during flight AC19. The black lines and shadings represent the median and inter-quartile range calculated for 150 m altitude bins during the flight section off the Brazilian coast (16:50 to 19:07 UTC, blue line in Fig. 1). The brown shaded area represents the approximate vertical location of the upper pollution layer (UPL). The altitudes of the lower pollution layer (LPL), the clean layer (CL), and the marine boundary layer (MBL) are indicated on the right-hand side of the plot. The precise time windows when the UPL, CL, LPL, and MBL were probed are shown in Table S1 of the Supplement.

to the LPL, CL, MBL, and fresh BB aerosols probed during AC19 – are shown in Fig. 4 and summarized in Table 2 (see Fig. S5 for individual PNSDs). A modal diameter of 132 nm was observed for the UPL aerosol, whereas the fresh BB aerosol showed a clearly smaller modal diameter of 124 nm. Further note that the modal diameter in the UPL is smaller than the 220 nm observed directly off the African coast (Weinzierl et al., 2011). The CCN concentrations at $S = 0.5\,\%$, $N_{\mathrm{CCN},0.5}$, show a maximum within the UPL with $N_{\mathrm{CCN},0.5} = 560 \pm 180\,\mathrm{cm^{-3}}$ as well as a high CCN fraction, $f_{\mathrm{CCN},0.5} = 60 \pm 6\,\%$ (Fig. 3d).

The N_{acc} within the UPL is lower than at the ATTO site under strongly BB-influenced ($N_{\mathrm{acc,BB}} \approx 3400\,\mathrm{cm^{-3}}$) and average dry season conditions ($N_{\mathrm{acc,dry}} \approx 1300\,\mathrm{cm^{-3}}$), yet still substantially higher than under an average wet season at ATTO ($N_{\mathrm{acc,wet}} \approx 150\,\mathrm{cm^{-3}}$) or pristine rain forest con-

Table 1. Characteristic aerosol and trace gas concentrations in the upper pollution layer (UPL), clean layer (CL), lower pollution layer (LPL), and marine boundary layer (MBL) observed during the AC19 flight section off the Brazilian coast (16:50 to 19:07 UTC; Fig. 1). For comparison, corresponding data from a fresh biomass burning plume (BB, also observed during AC19; see Fig. 1) have been added. Data are summarized as arithmetic mean ± standard deviation (SD) as well as 1st and 99th percentiles (P1 and P99).

	UPL				CL				LPL				MBL				BB			
	mean	SD	P1	P99	mean	SD	P1	P99	mean	SD	P1	P99	mean	SD	P1	P99	mean	SD	P1	P99
$N_{CN,20}$ (cm^{-3})	970	260	400	1500	500	60	450	760	1300	200	750	1750	420	140	220	800	4200	2100	1500	10 500
N_{acc} (cm^{-3})	850	330	260	1550	180	60	90	360	650	140	320	940	230	50	140	330	2700	1400	660	6600
$N_{CCN,0.5}$ (cm^{-3})	560	180	200	920	230	40	170	350	510	90	320	700	95	30	30	200	2000	1100	500	5100
N_{rBC} (cm^{-3})	280	110	90	530	30	12	9	60	110	20	60	190	50	16	24	84	280	110	120	630
f_{fine} (%)	15	14	0	45	65	7	44	79	48	11	27	69	43	13	18	68	37	8	19	61
f_{vol} (%)	16	9	3	40	43	6	25	55	27	7	13	44	39	9	22	62	17	7	2	38
$f_{rBC,N}$ (%)	28	5	17	40	6	2	2	11	9	2	5	14	12	3	5	19	7	2	4	11
$f_{CCN,0.5}$ (%)	60	6	44	71	46	6	34	62	41	8	26	59	23	6	11	38	45	5	31	54
c_{CO} (ppb)	150	30	100	210	83	4	78	101	105	5	96	115	92	1	90	94	162	40	107	277
c_{O_3} (ppb)	56	9	36	71	48	2	46	53	45	2	41	51	21	1	19	23	34	2	31	38
c_{NO_y} (ppb)	2.5	0.8	1.0	4.5	0.9	0.4	0.6	2.0	2.1	0.8	0.8	3.1	1.7	0.1	1.4	1.8	2.1	0.3	1.7	2.9
c_{NO} (ppb)	0.10	0.02	0.06	0.13	0.07	0.01	0.04	0.09	0.10	0.02	0.06	0.15	0.12	0.02	0.09	0.15	0.18	0.06	0.11	0.32
M_{rBC} (µg m^{-3})	1.0	0.4	0.3	2.0	0.09	0.05	0.02	0.25	0.36	0.11	0.17	0.73	0.17	0.07	0.07	0.37	0.70	0.24	0.35	1.36
M_{Org} (µg m^{-3})	2.5	1.2	1.2	4.4	0.91	–	–	–	1.72	0.15	1.57	1.86	−0.02	0.04	−0.08	0.04	4.6	1.6	2.2	7.4
M_{SO_4} (µg m^{-3})	0.86	0.41	0.50	1.60	0.42	–	–	–	0.79	0.02	0.76	0.81	0.22	0.08	0.14	0.33	0.57	0.18	0.38	0.94
M_{NO_3} (µg m^{-3})	0.33	0.26	0.08	0.70	0.04	–	–	–	0.05	0.02	0.03	0.07	0.013	0.012	−0.002	0.025	0.15	0.06	0.05	0.25
M_{NH_4} (µg m^{-3})	0.48	0.23	0.25	0.81	0.25	–	–	–	0.45	0.16	0.31	0.62	0.18	0.11	0.06	0.37	0.33	0.11	0.20	0.56

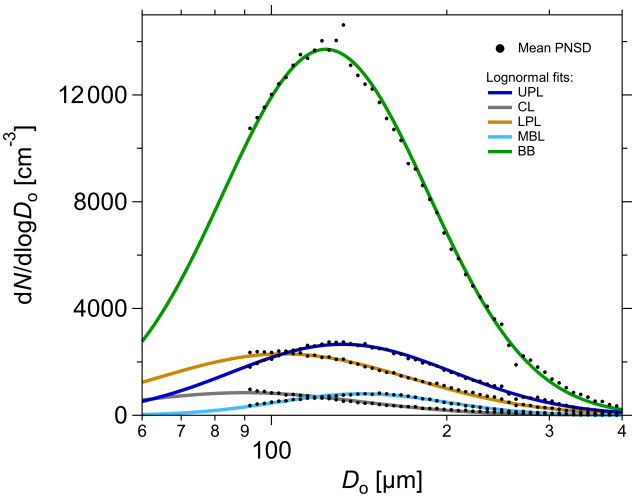

Figure 4. Particle number size distributions (PNSD) measured by the UHSAS for the UPL, CL, LPL, and MBL, as defined in Fig. 3, and the fresh BB plume probed during AC19 (see Fig. 1). The data points (black dots) are fitted by log-normal functions between 90 and 500 nm (Heintzenberg, 1994).

Table 2. Fit parameters of UHSAS-derived aerosol size distributions in Fig. 4, representing different conditions (i.e., layers, plumes) during AC19. A log-normal function (Heintzenberg, 1994) was used to fit a mono-modal size distribution to the mean data points: $\frac{dN}{d\ln d_p} = \frac{A}{\sqrt{2\pi}\ln\sigma_g}\exp\left(-\frac{(\ln d_p - \ln d_0)^2}{2\ln(\sigma_g)^2}\right)$.

	UPL	CL	LPL	MBL	BB
A	2920	970	2890	680	13 930
d_0 (nm)	132	90	105	143	124
σ_g	1.55	1.58	1.65	1.40	1.50
r^2	1.00	0.99	1.00	1.00	1.00

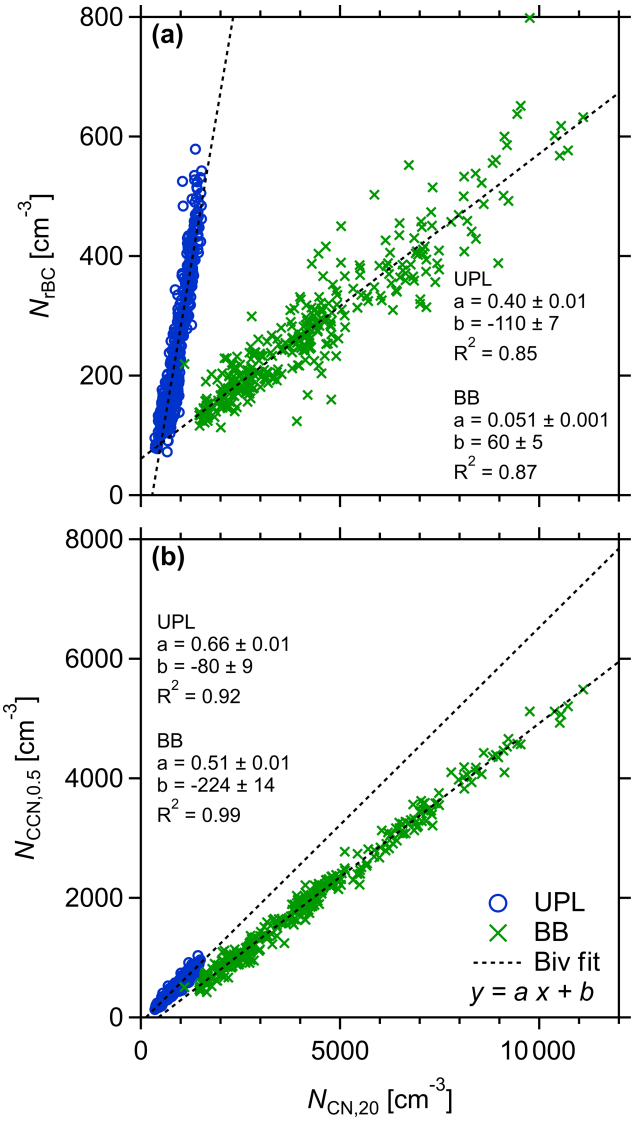

Figure 5. Correlation between **(a)** rBC particle number concentrations (N_{rBC}) and total aerosol ($N_{CN,20}$); and between **(b)** CCN at $S = 0.5\,\%$ ($N_{CCN,0.5}$) and total aerosol ($N_{CN,20}$) in the UPL (blue) and in the fresh biomass burning plume (green). The dashed lines are bivariate linear regressions applied to the data sets.

ditions ($N_{acc,PR} \approx 90\,cm^{-3}$) (Pöhlker et al., 2016, 2018). Remarkably, rBC particles represent a dominant species of the UPL aerosol population in terms of number concentration with $N_{rBC} = 280 \pm 110\,cm^{-3}$, corresponding to an rBC number fraction of $f_{rBC,N} = 28 \pm 5\,\%$ relative to $N_{CN,20}$ (Fig. 3e). The ratio $\Delta N_{rBC}/\Delta N_{CN,20} \approx 40\,\%$ in the UPL is much higher than $\Delta N_{rBC}/\Delta N_{CN,20} \approx 5\,\%$ in the fresh BB plume (Fig. 5a). Visually, the dark color of the layer observable in Fig. 2 corresponds to the high rBC fraction. For comparison, rBC number fractions of 0 %–15 % relative to $N_{CN,20}$ were observed in megacity pollution (Laborde et al., 2013) and $f_{rBC,N} \approx 6\,\%$ in wildfire plumes injected into the lowermost stratosphere in the Northern Hemisphere (Ditas et al., 2018).

In terms of absolute mass concentrations, rBC within the UPL, with $M_{rBC} = 1.0 \pm 0.4\,\mu g\,m^{-3}$ (ranging from 0.5 to $2\,\mu g\,m^{-3}$), approaches the highest BC levels observed at ATTO (M_{BC_e} up to $2.5\,\mu g\,m^{-3}$; Pöhlker et al., 2018; Saturno et al., 2018b). Figure 6 shows the fractions of rBC mass relative to the other main constituents of the submicrometer aerosol (M_{total} = non-refractory + rBC) in the UPL in comparison to the CL, LPL, MBL, and fresh BB values. Organic matter – comprising co-emitted primary as well as secondarily formed organics – accounts for the dominant mass fractions in all layers, with $f_{org,M} \approx 50\,\%$ in the UPL, CL, and, LPL, and as much as 72 % in the fresh BB plume. Generally, the dominance of organic matter is in agreement with previous studies performed at different locations and seasons in the Amazon region (e.g., Brito et al., 2014; Chen et al., 2015; Fuzzi et al., 2006; Martin et al., 2010, 2017; de Sá et al., 2019; Schneider et al., 2011; Schulz et al., 2018; Shrivas-

tava et al., 2019; Talbot et al., 1990). For example, in the southwestern region of the Amazon, which is heavily impacted by BB, organics account for $f_{\mathrm{org},M} > 90\,\%$ in the dry season (Brito et al.2014). Note that the thermal stability of some organic species and tar balls in BB plumes can lead to an underestimation of the $f_{\mathrm{org},M}$ measured by the C-ToF-AMS (Adachi et al., 2018). Further, the organic matter in the UPL is significantly more oxidized than the fresh BB smoke, as shown in Fig. S6. This can be associated with the long aging times and the elevated O_3 mixing ratio in the UPL (Fig. 3h) (Martin et al., 2017). The rBC mass fractions account for $f_{\mathrm{rBC},M} = 15\,\%$ in the UPL and $f_{\mathrm{rBC},M} = 12\,\%$ in the BB plume. A clear difference was observed for the mass fractions of the inorganic constituents sulfate (SO_4^{2-}), ammonium (NH_4^+), and nitrate (NO_3^-), which in sum account for $f_{\mathrm{inorg},M} = 35\,\%$ in the UPL and $f_{\mathrm{inorg},M} = 16\,\%$ in the BB plume. The increased $f_{\mathrm{inorg},M}$ in the UPL can probably be explained by aging-related condensation of the secondarily formed species SO_4^{2-}, NH_4^+, and NO_3^-. On the other hand, the lower $f_{\mathrm{org},M}$ in the UPL compared to the fresh Amazonian BB is related to the evaporation of organics due to fragmentation during the aging over the Atlantic. Note that, despite the higher $\Delta N_{\mathrm{rBC}}/\Delta N_{\mathrm{CN},20}$ in the UPL compared to the fresh BB (Fig. 5a), the UPL shows a higher CCN activated fraction ($\Delta N_{\mathrm{CCN},0.5}/\Delta N_{\mathrm{CN},20} = 66\,\%$, Fig. 5b). The high CCN efficiency is likely due to internal mixing of rBC with sulfate, nitrate, and highly oxygenated organic aerosol. These findings, in combination with the UPL's large geographic extent, suggest that it represents an aerosol and CCN reservoir of particular significance for the Amazonian cloud cycling and rainfall formation – i.e., cloud droplet formation and growth.

Regarding trace gases, Fig. 3g–j show absolute maxima in the UPL for the mole fractions of carbon monoxide (c_{CO}), ozone ($c_{\mathrm{O_3}}$), and total reactive nitrogen ($c_{\mathrm{NO_y}}$) as well as a secondary maximum for nitrogen monoxide (c_{NO}). The elevated $c_{\mathrm{CO}} = 150 \pm 30$ ppb along with the high M_{rBC} indicates that the UPL air masses originated from BB emissions. Moreover, the ratio between these two co-emitted species can be used as a tracer for the origin and age of BB plumes (Darbyshire et al., 2019; Guyon et al., 2005; Saturno et al., 2018b). The aged UPL is characterized by a higher rBC enhancement ratio, $\mathrm{EnR}_{\mathrm{BC},M} = 14.7 \pm 0.6\,\mathrm{ng\,m^{-3}\,ppb^{-1}}$, compared to fresh Amazonian BB with $\mathrm{EnR}_{\mathrm{BC},M}$ of $6.3 \pm 0.2\,\mathrm{ng\,m^{-3}\,ppb^{-1}}$ (Fig. S7). Recent aircraft measurements of African BB pollution over Ascension Island have found similar $\mathrm{EnR}_{\mathrm{BC},M} = 11$–$17\,\mathrm{ng\,m^{-3}\,ppb^{-1}}$ in the free troposphere (Wu et al., 2020). The ozone as a secondary pollutant also presents a maximum within the UPL ($c_{\mathrm{O_3}} = 56 \pm 9$ ppb) and appears to be anti-correlated with NO ($c_{\mathrm{NO}} = 0.10 \pm 0.02$ ppb). Therefore, the fact that O_3 and NO_y ($c_{\mathrm{NO_y}} = 2.5 \pm 0.8$ ppb) are strongly enhanced in the pollution layers reflects the high photochemical age of the plume. Overall, the trace gas mole fractions within the UPL are consistent with previous aircraft measurements. Over the Atlantic, off the city of Natal, Brazil, Andreae et al. (1994) found similar pollution layers with $c_{\mathrm{O_3}}$ and c_{CO} up to 90 and 210 ppb, respectively. The mean mole fraction of NO_y in these plumes was extremely high: 4.4 ± 3.1 ppb, with enhancement ratios, $\mathrm{EnR}_{\mathrm{NO_y}}$, in the range 0.018 to 0.108. The $\mathrm{EnR}_{\mathrm{NO_y}}$ in the UPL (0.019) lies in the lower part of this range. Over Ascension Island, $c_{\mathrm{O_3}}$ can be as high as 80 ppb in the lower troposphere (Thompson et al., 1996).

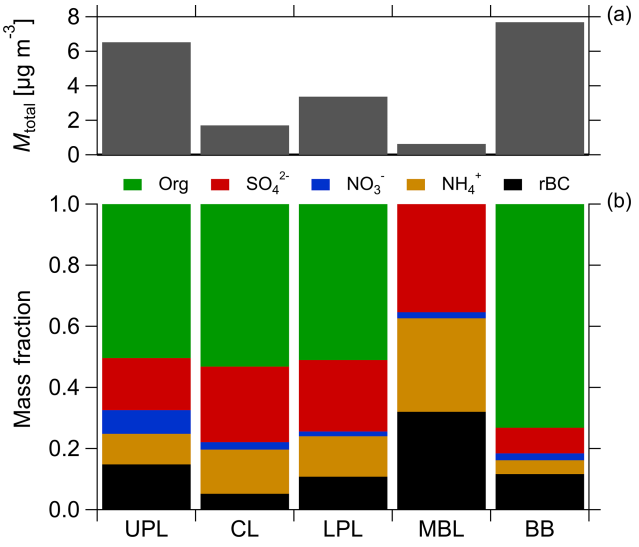

Figure 6. Cumulative mass concentrations of non-refractory submicrometer species (i.e., organic (Org), sulfate (SO_4^{2-}), nitrate (NO_3^-), ammonium (NH_4^+)) and rBC **(a)**; and mass fractions of the respective species to the total mass ($M_{\mathrm{total}} = M_{\mathrm{Org}} + M_{\mathrm{SO_4}} + M_{\mathrm{NO_3}} + M_{\mathrm{NH_4}} + M_{\mathrm{rBC}}$) in the UPL, CL, LPL, and MBL, as defined in Fig. 3, and the fresh BB plumes probed during AC19 (see Fig. 1) **(b)**. Note that no C-ToF-AMS data were available from 17:27 to 19:05 UTC during the offshore section of flight AC19 and, therefore, a reduced number of measurements points are included in the averages. The concentration of organics was below the detection limit in the MBL.

Below the UPL, the atmospheric vertical profile off the Brazilian coast shows a second maximum in aerosol concentrations in the LPL ($N_{\mathrm{CN},20} = 1300 \pm 200\,\mathrm{cm^{-3}}$; $N_{\mathrm{acc}} = 650 \pm 140\,\mathrm{cm^{-3}}$) at altitudes between ~ 2.3 and 3.0 km (Fig. 3). The properties of the UPL and LPL, however, are remarkably different. The LPL shows rather lower concentrations of rBC ($M_{\mathrm{rBC}} = 0.36 \pm 0.11\,\mathrm{\mu g\,m^{-3}}$ and $N_{\mathrm{rBC}} = 110 \pm 20\,\mathrm{cm^{-3}}$), CO ($c_{\mathrm{CO}} = 105 \pm 5$ ppb), and O_3 ($c_{\mathrm{O_3}} = 45 \pm 2$ ppb), which decreases with decreasing altitude. NO_y actually reaches the highest concentrations in this layer, with values up to 3.0 ppb. We assume that the pyrogenic species found in the LPL are also advected from Africa; however, possible influences from urban emissions in Africa and/or South America, for example, should not be neglected. This possibility is supported by the relatively high sulfate content of the aerosol in this layer, which at an average value of $0.79 \pm 0.02\,\mathrm{\mu g\,m^{-3}}$ accounts for 23 % of the total aerosol mass concentration (Fig. 6). Sulfur-rich anthropogenic emis-

sions from fossil-fuel combustion may have become mixed with BB emissions by cloud venting over the Gulf of Guinea region (Dajuma et al., 2019).

One interesting aspect of the LPL is that the ultrafine fraction accounts for about half of the aerosol number concentration ($d_0 = 105$ nm; see PNSD in Fig. 4). Likewise, in the LPL the f_{vol} is higher than in the other atmospheric levels. One possible explanation for this is that new particle formation occurs in the detrainment regions around the shallow cumulus, which brings air masses from the marine boundary layer (MBL), containing dimethyl sulfide and SO_2, into the LPL. This phenomenon has previously been reported by several authors (Hegg et al., 1990; Kerminen et al., 2018; Perry and Hobbs, 1994). Direct convective transport of ultrafine particles from the MBL into the LPL is unlikely to be an important source of such particles, as their concentration in the MBL is only about 200 cm^{-3}, well below their concentration in the LPL of about 700 cm^{-3}. In the MBL (with its top at $\sim$ 600 m a.s.l.), the total and accumulation-mode particle concentrations are somewhat lower than in the layers aloft ($N_{CN,20} = 420 \pm 160$ cm^{-3} and $N_{acc} = 230 \pm 50$ cm^{-3}) and present larger diameters ($d_0 = 143$ nm). The MBL appears to be only weakly influenced by the African BB, with $M_{rBC} = 0.17 \pm 0.07$ $\mu g\, m^{-3}$ and N_{rBC} accounting for only 10 % of the $N_{CN,20}$. Additionally, the aerosol population in the MBL appears less efficient as CCN, with only 20 % of particles being activated at $S = 0.5$ % (Fig. 3d).

In between the UPL and LPL, the $\sim$ 200 m thick CL was found centered at $\sim$ 3.2 km altitude with relatively dry air as represented by a sharp decrease in q. Such clean layers have been previously observed in the dry season over the African continent and adjacent oceans, specifically in the southeastern Atlantic Ocean, with a few hundred (up to 1 km) meters thickness (Hobbs, 2003). Within the CL, the combustion tracer concentrations M_{rBC}, N_{rBC}, and c_{CO} sharply decrease to 0.09 ± 0.05 $\mu g\, m^{-3}$, 30 ± 12 cm^{-3}, and 83 ± 4 ppb, respectively. We further found $N_{CN,20} = 500 \pm 60$ cm^{-3}, which is comparable to $N_{CN} = 500$ cm^{-3} in another CL as reported by Hobbs (2003). Within the CL, the aerosol size distribution is substantially shifted towards the Aitken mode ($d_0 =$ 90 nm, Fig. 4). The c_{O_3} shows a slight decrease to 48 ± 2 ppb. Hobbs (2003) proposed that the CL derived from the ultraclean upper tropospheric air.

In the vicinity of the western African coast, similar tropospheric stratification was observed in a recent aircraft campaign. Aerosol and trace gas profile measurements over the Gulf of Guinea in July 2016, measured under the influence of aged BB plumes originating in central Africa, revealed two distinct aerosol layers, where the upper one, centered at 3.8 km altitude, was enriched in rBC (~ 0.3 $\mu g\, m^{-3}$), CO ($\sim$ 340 ppb), and organics (~ 65 $\mu g\, m^{-3}$) (Denjean et al., 2019; Flamant et al., 2018). Moreover, Weinzierl et al. (2011) reported $f_{vol} = 26$ % (13 %–52 %, p_3–p_{97}) for BB plumes near the western African coast in 2008 during SAMUM-2, which are larger than the f_{vol} within the UPL in this study. Typically, organic aerosol becomes less volatile during atmospheric aging, concurrent with an increase in its O/C ratio (Grieshop et al., 2009; Isaacman-VanWertz et al., 2018; Slowik et al., 2012; Zhou et al., 2017). More recently, from comprehensive measurements on Ascension Island in the middle of the South Atlantic, Zuidema et al. (2018) described a smoke layer over a stratocumulus cloud deck where "shortwave-absorbing aerosol emanating from biomass burning in continental Africa advects westwards over the South Atlantic for approximately one third of the year, from June to October". These previously reported results suggest that the discrete rBC-enriched layer reported here likely formed in the vicinity of the African coast and tapered as it approached the South American continent. In addition, the atmospheric stability facilitated the transport across the South Atlantic towards the Amazon. Further, ongoing studies suggest the existence of a low-level jet with a maximum around 800 hPa ($\sim$ 3 km) induced by changes in boundary layer height during the day (Anselmo et al., 2020). The low-level jet may be the main mechanism transporting the African pollution from the Atlantic Ocean into the Amazon Basin.

3.2 Backward trajectories and potential source regions in Africa

Based on BTs, which reflect the large-scale trade wind circulation patterns, we investigated the origin and age of the UPL up to 10 d prior to its observation. Figure 7a compares BT ensembles – started in the relevant offshore area (i.e., 3° N to 3° S; 52 to 44° W) and during the time period of the UPL observation by the aircraft (i.e., 30 September 2014 18:00 UTC) – for the starting heights at 500 m (representing near-surface conditions), 2500 m (peak of LPL), 3500 m (peak of the UPL), and 5000 m above ground level (well above the UPL). The comparison of the different BT starting heights shows clear differences in air mass advection patterns: specifically, the UPL BTs indicate rather fast and directed air mass movements from easterly directions, whereas the LPL BTs indicated more curvilinear movement from east-southeasterly directions. The fact that the BT patterns diverge is consistent with the different trace gas and aerosol properties shown in Fig. 3, underlining that LPL and UPL represent air masses of different origin and/or atmospheric aging history. Furthermore, the wind fields at about 3500 m illustrate the large-scale meteorology at the UPL altitude. The transatlantic transport time of the UPL air masses was about 10 d according to the BT ensembles.

The fire map in Fig. 7a helps to identify potential source regions of the UPL aerosol. It includes fires within a 5 d window (15 to 20 September 2014) of when the BB-laden air masses likely originated in the African source regions and then started their $\sim$ 10 d journey across the Atlantic Ocean until the aircraft observation on 30 September. Several hotspots of fire activity in central and southern Africa can be found in Fig. 7a_1. All of them are located in tropical and

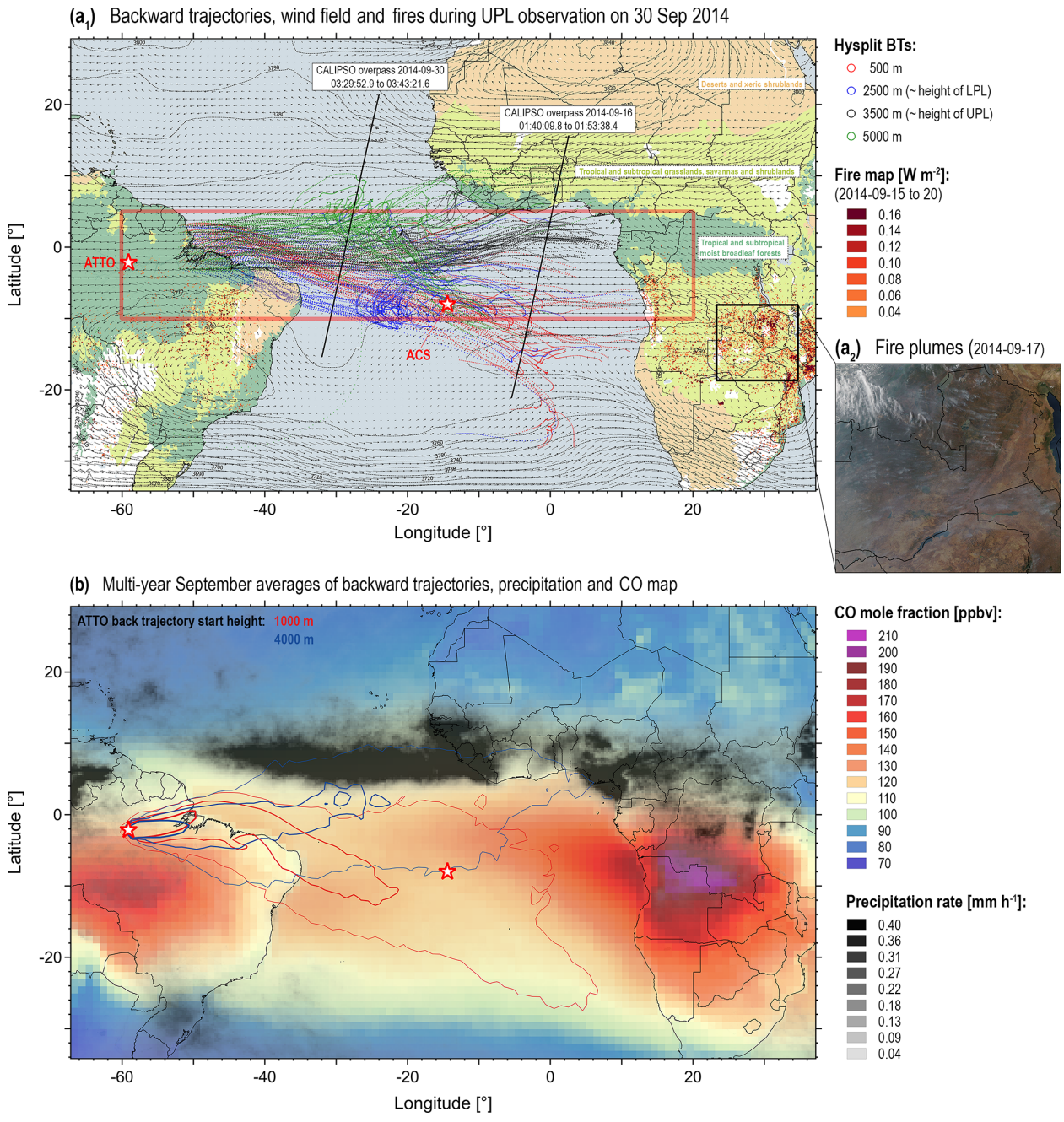

Figure 7. Composite maps combining backward trajectories (BTs) and satellite data products characterizing atmospheric conditions **(a_1)** during flight AC19 on 30 September 2014 in comparison to **(b)** the averages of September observations during multiple years. Panel **(a_1)** shows HYSPLIT 10 d BTs starting at different altitudes (500, 2500, 3500, 5000 m a.g.l.) at 18:00 UTC on 30 September 2014 (similar time and location to the UPL observations during flight AC19). Note that the altitudes where the BTs were initiated include the heights of the sampled UPL and LPL. The fire radiative power (FRP) density (mW m^{-2}), retrieved by the Global Fire Assimilation System (GFAS v1.0) averaged from 15 to 20 September 2014, is also shown as a fire map with $0.1° \times 0.1°$ grid resolution. The orbits of two CALIPSO passages on 30 and 16 September 2014 as shown in Fig. 9 as well as the geographic locations of the ATTO site and Ascension Island are also illustrated. Panel **(a_2)** shows multiple clearly visible fire plumes in the African source region. Panel **(b)** shows multi-year averages of all Septembers for (i) HYSPLIT BT ensembles starting at ATTO (1000 and 4000 m a.g.l.) from 2005 to 2018. Contour lines represent the fraction of occurrence of overpassing trajectories in a specific region as described in Pöhlker et al. (2019). (ii) AIRS-derived CO data products (400 to 600 hPa atmospheric levels) from 2005 to 2018 and (iii) TRMM precipitation from 2005 to 2018. For general illustration, animations (https://climate.nasa.gov/climate_resources/146/video-simulated-clouds-and-aerosols/, last access: 4 July 2019; https://gmao.gsfc.nasa.gov/research/aerosol/modeling/nr1_movie/, last access: 4 July 2019) of the Goddard Earth Observing Model (Version 5, GEOS-5) show that aerosol particles are transported efficiently from Africa to South America and to a lesser extent from South America to Africa (Colarco et al., 2010; Yasunari et al., 2011).

subtropical grasslands, savannas, and shrublands according to Olson et al. (2001). Particularly, the Miombo woodlands are well known as a region of frequent and intense fire activities, mostly driven by human activities (Andela and van der Werf, 2014; Barbosa et al., 1999; Earl et al., 2015). For the time frame of 15 to 20 September 2014, satellite-based natural color reflectance images show the high fire activity through a larger number of clearly visible smoke plumes in the hotspot areas (one example is shown for 19 September 2014 in Fig. $7a_2$). Note that at the same time, the fire activity in South America is still comparatively low (Fig. $7a_1$). Overall, the fires, wind field, and BTs in Fig. $7a_1$ show a coherent picture and suggest that the shown grassland, savanna, and shrubland fires represent the sources for the UPL at the Brazilian coast.

It has been generally assumed – though not shown in detail and quantified yet – that African smoke accounts for a significant fraction of pollution input into the Amazon Basin (Saturno et al., 2018b). Therefore, we complemented the case-specific map in Fig. $7a_1$, which focuses on the precise time window of flight AC19, by a seasonally averaged map in Fig. 7b, presenting the multi-year September averages of CO (the complete yearly cycle is shown in Fig. S8). The map in Fig. 7b emphasizes the large extent of the African smoke plume (here represented by CO) over the Atlantic area. It further shows good agreement between the CO plume pattern and BT ensembles at the central Amazonian ATTO site, indicating that transatlantic smoke transport is a general and seasonally recurring phenomenon beyond the specific case of the analyzed layer in September 2014. This is supported by in situ measurements made during the Atmospheric Tomography mission (ATom) 2016–2018 flight missions, which showed elevated concentrations of BB aerosols (about 0.1 to 1 $\mu g\,m^{-3}$) over most the of the southern tropical Atlantic in July to October (Schill et al., 2019). Biomass smoke particles were the dominant aerosol fraction in this region between the surface and 4 km altitude. Further note that precipitation rates over the South Atlantic are comparatively low, as shown in Fig. 7b. Accordingly, rain-out and wash-out mechanisms likely do not substantially reduce the BB aerosol population during transport.

3.3 Geographic extent of pollution layers over the Atlantic and direct radiative effects

Satellite-based observations resolve the transatlantic transport of the pollution layers. Figure 8 illustrates the movement of the African aerosol particles across the Atlantic by means of the burning tracer CO, where individual plumes during the dry season of 2014 can be identified. This includes the plume probed at the Brazilian coast during AC19 (marked by a dashed line), which appears to be coincidentally the strongest plume in 2014. Beyond this particular event, several weaker plumes were also observed. Based on Fig. 8, a characteristic transport velocity of $\sim 380\,km\,d^{-1}$ can be

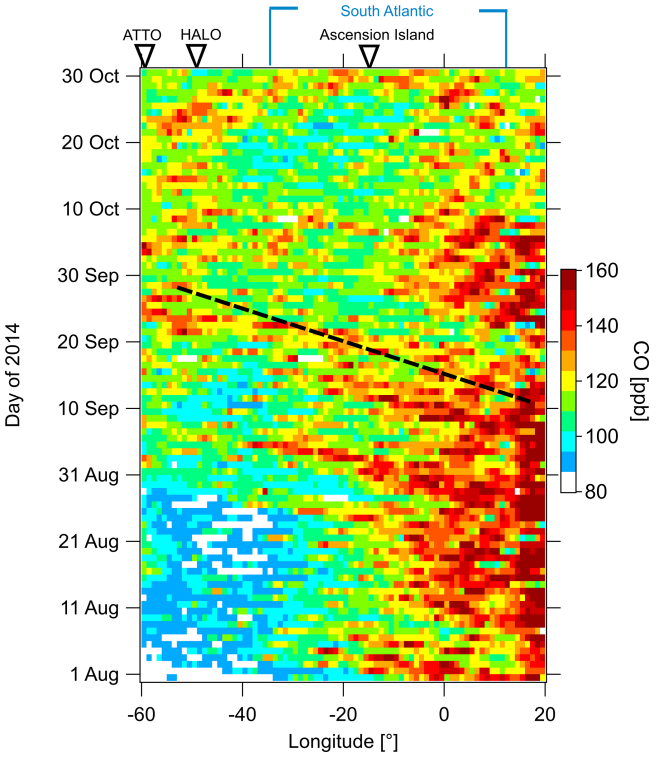

Figure 8. Hovmöller plot of the daily AIRS-derived carbon monoxide (400 to 600 hPa) distributed over the South Atlantic region (60° W to 20° E) from August to October 2014, averaged over the latitudinal band of 10° S to 5° N, corresponding to the region of interest (ROI) highlighted in Fig. $7a_1$. Several events of transatlantic transport of aerosol from Africa towards South America can be identified. The black dashed line highlights a particularly strong plume originating around 10 September 2014 and arriving in the observational area of AC19 on 30 September.

obtained and, therefore, an aging time of ~ 10 d. Similarly, satellite-based AOD observations can be used to resolve the plume movement as shown in Fig. S9.

The transatlantic transport of the particular BB plume that was probed during AC19 was temporally and geographically close to that of a volcanogenic sulfate-rich plume, whose origin was related to a period of strong activity of the Nyamuragira volcano in the eastern Democratic Republic of the Congo. The associated major SO_2 emissions were oxidized to sulfate during the transatlantic passage (Saturno et al., 2018a). The plume of sulfate-rich aerosols was observed airborne during ACRIDICON-CHUVA flight AC14 on 21 September 2014 in the region from 200 to 400 km south of Manaus as well as by ground-based measurements at ATTO from 21 to 30 September 2014. Importantly, the BB plume probed during AC19 and the volcanogenic plume probed during AC14 were distinct events (i.e., did not occur in the same air masses) since the volcanogenic plume (i) occurred ~ 1 week earlier, (ii) was observed to be strongest between 4 and 5 km, in contrast to 3 to 4 km for the BB

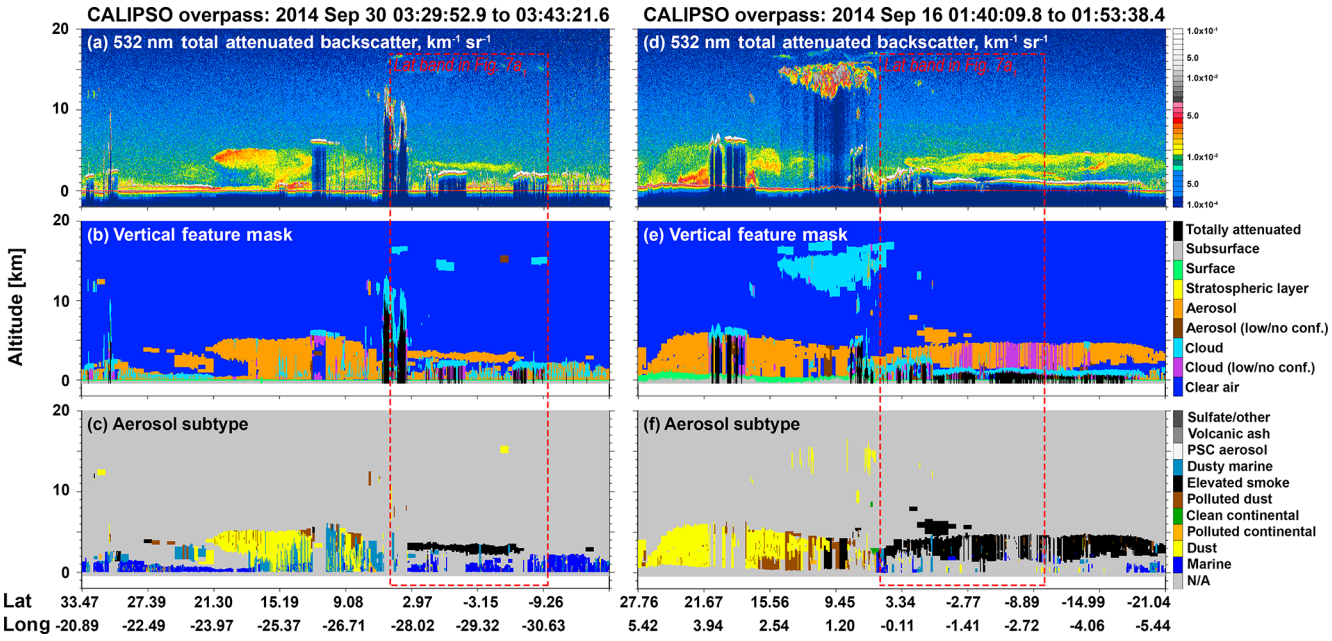

Figure 9. CALIPSO-derived lidar profiles for 16 and 30 September 2014, where African BB plumes were identified over the South Atlantic Ocean. The first profile near the South American coast shows the aerosol layer at similar altitudes to those observed during flight AC19. Satellite orbits for both profiles are shown in Fig. $7a_1$.

plume, and (iii) showed a very low rBC mass concentration. However, the volcanogenic plume can be regarded as a "reference case of the dynamics and conditions of transatlantic aerosol transport from southern Africa to South America" (Saturno et al., 2018a). The temporal coincidence of the volcanogenic and BB plumes suggests that transatlantic aerosol transport was particularly efficient in the second half of September 2014. Moreover, the observation that the single volcanogenic plume significantly influenced the aerosol particle chemical composition, hygroscopicity, and optical properties at ATTO (Saturno et al., 2018a) suggests that the more frequent and presumably stronger African BB plumes likely have a similarly profound impact on the central Amazonian aerosol population, at least during the dry season.

The African BB plumes (particularly the strong event at the end of September) were also observed by the vertically resolved aerosol extinction measurements by the CALIPSO satellite, revealing elevated and vertically defined smoke layers over the South Atlantic. Figure 9 shows two selected CALIPSO passages on 16 and 30 September 2014 (the day of the AC19 flight). More examples of similar layers over the Atlantic Ocean in September 2016 are shown and discussed in Barkley et al. (2019). These passages show exemplary snapshots of the elevated smoke layers at different longitudinal locations: on 16 September 2014 a layer was probed relatively close to the southern African coast, whereas on 30 September 2014 a layer was observed halfway between Ascension Island and the Amazon River delta. For the overpass on 30 September 2014, the layer's N–S extension was about 1200 km and its altitude between 3 and 4 km, which agrees well with the altitude of the UPL observation during flight AC19. For the passage on 16 September 2014, the layer's N–S extension was about 4° N to 20° S (∼ 2800 km) and its altitude between 2 and 5 km. In this context, a dedicated study of Adebiyi and Zuidema (2016) has shown that 45 % of the forward trajectories of satellite-detected smoke plumes in southern Africa exit the continent westwards between 5 and 15° S and are transported westward by the Southern African Easterly Jet (AES-J), overlying a semi-permanent marine stratocumulus deck. Moreover, Fig. 9 suggests that the layer's latitudinal extent decreases as it approaches the South American continent.

In order to constrain the seasonal and vertical aspects of the transatlantic transport, we analyzed the satellite-retrieved aerosol profiles over the South Atlantic Ocean during the dry season of multiple years (2012 to 2018). Figure 10a–c show the extinction coefficients of all CALIPSO overpasses within the region of interest (ROI, as defined in Fig. 7a) averaged over the months of August, September, and October. High aerosol loadings (up to 5 km altitude) in the longitude band from 10 to 20° E correspond to BB emissions over the African continent. Likewise, comparably high extinction coefficients (up to 3 km altitude) are observed due to BB fires in South America (60 to 40° W). Over the South Atlantic from 40° W to 10° E, the maximum extinction coefficient is observed at two different levels of the atmosphere, separated by a relatively clean layer in between. The lower layer (altitude < 1 km) with a pronounced extinction coefficient rep-

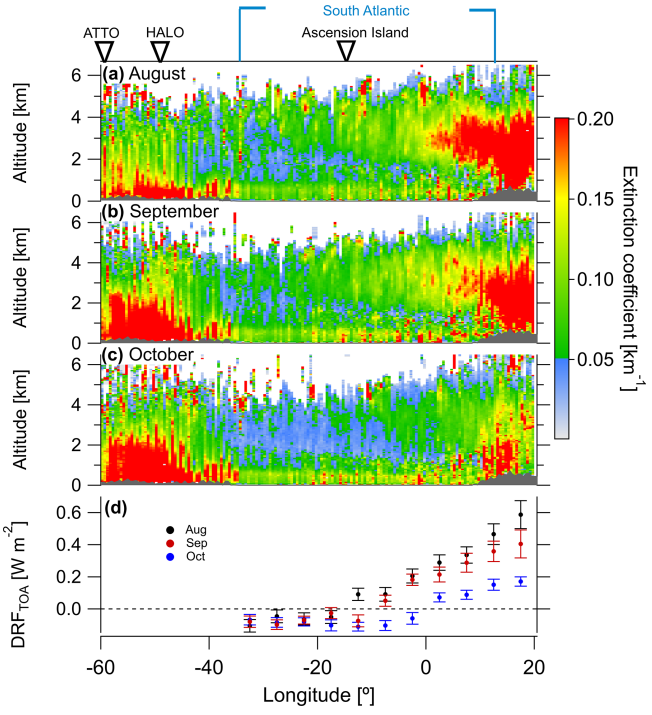

Figure 10. Curtain plot showing the columnar aerosol extinction coefficient at 532 nm, based on multi-year CALIOP data from 2012 to 2018 (only nighttime data). Panels represent monthly averages for the months of **(a)** August, **(b)** September, and **(c)** October within the latitude band from 10° S to 5° N, corresponding to the ROI indicated in Fig. 7a$_1$. The grey shaded area represents the mean surface elevation and depicts boundaries of the African and South American continents. Panel **(d)** shows the daily mean of the direct radiative forcing at the top of the atmosphere (DRF-TOA) exerted by the pollution layer over the South Atlantic Ocean, calculated using the LibRadTran radiative transfer model.

resents the MBL, which is presumably dominated by the (coarse-mode) marine aerosols and is clearly visible throughout the 3 months in Fig. 10. On the other hand, the higher layer (altitudes between 1 and 5 km) represents the African BB aerosol being transported westwards over the Atlantic all the way to South America. The transport pattern stands out in the months of August and September, but is weakened in October, when the remaining BB plumes appear to be mostly/completely removed from the atmosphere halfway before reaching South America. The injection height of BB aerosol in Africa is relatively high due to the AEJ-S, which induces an upward motion directly below the jet, enhancing updrafts over land that lift up BB aerosols to altitudes where they can be efficiently transported over the South Atlantic (Adebiyi and Zuidema, 2016). The vertical location of pollution plumes in the atmosphere is an important parameter, as it can considerably influence its atmospheric lifetime. Aerosol lifted up to higher altitudes tends to be advected over larger distances due to less efficient removal mechanisms (i.e., wet deposition). When leaving the African coast, the smoke layer is present at altitudes between 1.5 and 5 km, but becomes more restricted to higher altitudes (3–5 km) as it moves towards South America. Figure 10 suggests a pronounced thinning of the layer during its movement westwards due to dilution.

The transatlantic transport pattern of African BB, as presented here, is not well represented by the state-of-art atmospheric models. The simulations of the transatlantic transport of BB aerosol by several global aerosol models are able to capture the vertical distribution of aerosol over the African continent, but diverge from the satellite observations as it moves westward over the Atlantic Ocean (Das et al., 2017). In the models, BB aerosol plumes quickly descend to lower levels just off the western African coast, while our observations suggest that they are transported at high altitudes (< 5 km) well above the MBL all the way to the Amazon Basin. After reaching the Brazilian coast, the smoke layer gradually subsides, likely being entrained into the cloud layer below or more deeply mixing into the boundary layer. The effects of the aged pollution plume on radiative and cloud-nucleation properties over the Atlantic and upon arrival in the Amazon Basin are still uncertain.

In order to estimate the direct radiative effect that the African BB layer exerts along its transport over the Atlantic, we used the mean CALIPSO profiles to obtain information about the vertical extent of the plumes. Figure 10d shows the longitudinal profile of DRF-TOA calculated for different AOD values and atmospheric conditions as daily mean values for 3 different months. We observed a decrease in the warming effect of the aerosol towards South America. Near the African coast, a positive DRF-TOA was observed, reaching values as high as $+0.6\,\mathrm{W\,m^{-2}}$ in August, $+0.4\,\mathrm{W\,m^{-2}}$ in September, and $+0.17\,\mathrm{W\,m^{-2}}$ in October. On the other hand, negative DRF-TOA, ranging from -0.03 to $-0.10\,\mathrm{W\,m^{-2}}$, was found through the 3 months for lower AOD values (longitudes $< 5°$ E). The change in sign of the DRF-TOA is mostly a result of the high amount of absorption assumed for the aerosol layer in the simulations (single scattering albedo of 0.84). At higher optical depths, the absorption in the layer dominates, thus causing a positive forcing (warming) at TOA. At low AOD values, on the other hand, the absorption is weaker and the back-scattered radiation dominates the radiative effect, resulting in a negative aerosol radiative forcing at the TOA. Sensitivity cases for different assumptions about aerosol and surface properties are shown in Fig. S10. Our results suggest that the transport of BB smoke across the Atlantic has strong direct effects on the regional radiative balance, which changes from warming to cooling along the way from southern Africa to South America.

3.4 Transport of the pollution layer into the Amazon Basin

An important question for the aerosol cycling in the Amazonian troposphere is how the UPL evolves as it moves from

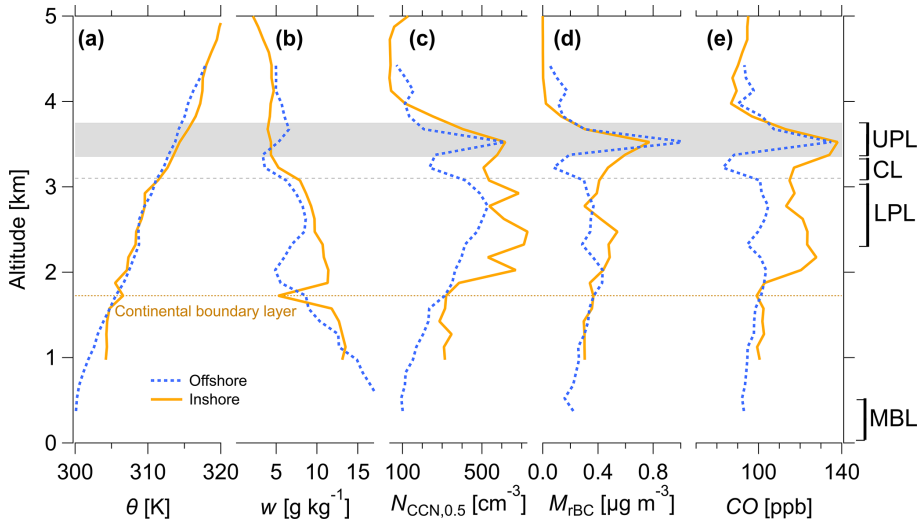

Figure 11. Vertical profiles of selected meteorological, aerosol, and trace gas parameters measured inshore and offshore of the Brazilian coast during AC19: **(a)** potential temperature, θ; **(b)** water vapor mass mixing ratio, w; **(c)** CCN ($S = 0.5\,\%$) number concentration, $N_{\mathrm{CCN},0.5}$; **(d)** rBC mass concentration, M_{rBC}; and **(e)** carbon monoxide mole fraction, c_{CO}. The figure shows the medians calculated for 150 m altitude bins over the flight sections inshore (yellow) and offshore (blue) of the Brazilian coast (as indicated in Fig. 1). The grey shaded area represents the approximate vertical location of the upper pollution layer (UPL) and the grey dashed line the lower limit of the clean layer (CL) observed exclusively during the offshore profiles.

the Atlantic Ocean into the South American continent. With the data available from flight AC19 (six offshore and two onshore penetrations of the UPL, Fig. 1), at least some conclusion can be drawn for the first ~ 400 km of UPL (as well as CL and LPL) transport over land. Figure 11 overlays onshore vs. offshore vertical profiles of selected meteorological, aerosol, and trace gas parameters. Meteorologically, the θ profiles show some divergences between inshore and offshore in the well-mixed continental boundary layer (up to ~ 1.5 km altitude) and in the UPL altitude band. Even stronger differences were found in the q profiles, which show the broadening of the upper dry layer from offshore to onshore profiles. Regarding the CL, the characteristic trace gas and aerosol concentration minima in the offshore profiles mostly disappeared onshore (e.g., for CCN, M_{rBC}, and c_{CO}, Fig. 11c, d, e). This fading of the CL minimum appears to be linked to the evolution of the UPL's vertical structure, which mostly remains intact, showing however a tendency to broaden and subside into the altitude range of the CL (i.e., 3.1 to 3.3 km), likely because of the onset of deeper vertical convective mixing over land. In addition, the inshore profiles also suggest that some BB emissions have been added, as the air masses moved inland because the increased concentrations of CCN, rBC, and CO in the LPL cannot be explained by downward mixing from the UPL alone. This is consistent with the presence of scattered fires in the coastal region (Fig. 1).

In this context note that a pronounced UPL was exclusively observed during flight AC19 (the only flight over the northeastern basin), whereas no comparable stratification was found during the other 13 flights in the central and western parts of the basin (Wendisch et al., 2016). Also, upon ascent after take-off and descent before landing of AC19 at Manaus International Airport, the altitude range (i.e., 3 to 4 km) was probed; however, no clear indications of an UPL were found. This suggests that the UPL started broadening over the first 400 km over the continent and faded away when the air masses reached the central basin in the region of Manaus (~ 1200 km from the coast). Accordingly, we conclude that convective mixing by the abundant cumulus that typically reaches up to 4–6 km over the Amazon prevented a well-defined UPL from being preserved far into the central basin. As a result, the aerosol brought in by the UPL is mixed downwards through convection and then transported further westwards with the boundary layer air masses. Similar downward mixing of BB emissions by convection over land has been reported from the south of western Africa (Dajuma et al., 2019).

3.5 Estimated relevance of the pollution layer for central Amazonian aerosol cycling

Considering the large horizontal extension of the pollution layer, it presumably accounts for an important input of aerosols and trace gases into the Amazon Basin, with potentially strong impacts for cloud microphysics as well as the atmospheric radiative budget. Here we put the experimental results outlined so far into a broader context of multiple years of observations at the central Amazonian ATTO site to estimate the relevance of the pollution layer input for

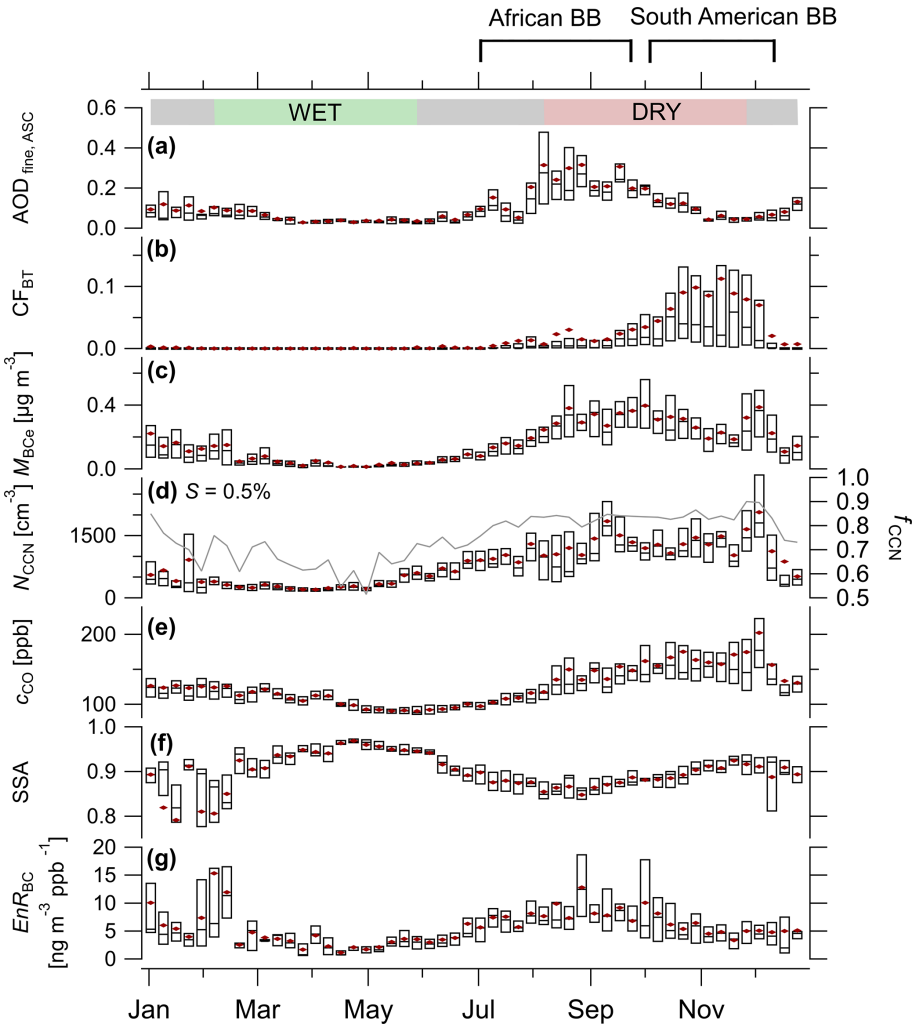

Figure 12. Seasonality of aerosol and trace gas properties based on long-term observations (2013–2018) at Ascension Island **(a)** and at the ATTO site **(b–g)**. The plot shows **(a)** fine-mode aerosol optical depth (AOD_{fine}) at 500 nm retrieved by the AERONET sunphotometer at Ascension Island; **(b)** cumulative fire intensity along the backward trajectories (CF_{BT}) of air masses arriving at the ATTO site (for details, see Sect. 2.6); **(c)** black carbon mass concentration M_{BC_e}; **(e)** CCN concentrations and activated fraction at $S = 0.5$ %; **(e)** CO mole fraction; **(f)** single scattering albedo, SSA; and **(g)** BC enhancement ratio, EnR_{BC}. The boxplots represent weekly statistics with the mean (red markers), the median (segment), and the 5th and 75th percentiles (lower and upper box edges) of the long-term daily measurements. The green and red shaded areas represent the wet and dry seasons, with transition periods in between, as defined in Pöhlker et al. (2016). On the top of the figure, markers indicate periods within the BB-influenced part of the year that ATTO is dominated either by the LRT of African BB or by the South American BB.

the central Amazonian aerosol lifecycle. Therefore, Fig. 12 combines the seasonal variability of relevant parameters to assess the interplay of African vs. South American BB emissions for the observed aerosol abundance and properties at ATTO. The influence of African BB transport into the basin is represented by the fine-mode AOD at Ascension Island, $AOD_{fine,ASC}$, based on ~ 20 years of AERONET observations. Note that Ascension Island is located in the main BT path of the transatlantic pollution transport and therefore a well-located observational site *en route* (Fig. 7a$_1$). The influence of South American BB for the ATTO observations is represented by a BT data product, CF_{BT}, based on pixel-wise accumulation of fire intensities along individual ATTO BTs over a multi-year period.

Generally, the Amazonian atmosphere is strongly influenced by BB aerosols during the dry season and to a somewhat lower extent during the flanking transition periods, causing significant increases in scattering and absorption coefficients (Rizzo et al., 2013; Saturno et al., 2018b). In Fig. 12, the long-lasting BB influence can be seen by means of the broad seasonal maxima in M_{BC_e}, $N_{CCN,0.5}$, and c_{CO}. The BB-impacted part of the year in the Amazon, including dry season and transition periods, will be called hereafter the BB season. Remarkably, the African BB influence (repre-

Table 3. Characteristic aerosol and trace gas concentrations during the African vs. South American dominated periods of the BB season at the ATTO site: arithmetic mean ± SD, median and inter-quartile range of daily averages from 2013 to 2018.

	African dominated BB[b]					South American dominated BB[c]				
	mean	SD	median	25th perc	75th perc	mean	SD	median	25th perc	75th perc
$N_{CN,20}$ (cm^{-3})	1350	550	1300	900	1700	2000	1000	1800	1400	2300
$N_{CCN,0.5}$ (cm^{-3})	1100	500	1090	750	1400	1800	900	1600	1200	2000
M_{BC_e} ($\mu g\,m^{-3}$)	0.36	0.12	0.33	0.26	0.42	0.41	0.17	0.36	0.29	0.48
c_{CO} (ppb)	140	30	131	120	150	190	70	170	150	200
$f_{CCN,0.5}$ (%)	83	6	84	80	87	87	04	88	84	90
EnR_{BC}[a] ($ng\,m^{-3}\,ppb^{-1}$)	11	6	10	7	14	6	4	5	3	7
SSA (637 nm)	0.85	0.02	0.85	0.84	0.86	0.90	0.03	0.90	0.89	0.93

[a] Daily EnR_{BC} (from 2013 to 2018) was calculated by applying a bivariate fit to 30 min averages of M_{BC_e} and c_{CO} measurements (see Sect. 2.3). [b] To calculate the African BB dominated state, periods with South American fire influences (CF_{BT} > 50th percentile of $CF_{BT,dry}$) and with clean atmospheric conditions (M_{BC_e} < 50th percentile of $M_{BC_e,dry}$) were excluded. [c] To calculate the South American BB dominated state, we selected periods with South American fire influences (CF_{BT} > 50th percentile of $CF_{BT,dry}$) and with polluted atmospheric conditions (M_{BC_e} > 50th percentile of $M_{BC_e,dry}$).

sented by $AOD_{fine,ASC}$) vs. the South American BB influence (represented by CF_{BT}) shows contrasting and complementary seasonal cycles: $AOD_{fine,ASC}$ has its onset in July, peaks in September, and drops again in October (see also Figs. 8 and 10), whereas CF_{BT} has its onset in September, peaks in October/November, and drops towards the beginning of December. The seasonal cycles in M_{BC_e}, $N_{CCN,0.5}$, and c_{CO} vs. $AOD_{fine,ASC}$ and CF_{BT} in Fig. 12 suggest that the Amazonian BB season can be regarded as consisting of an African-smoke dominated period in the first half and an South American-smoke dominated period in the second half of this season. In fact, differences between the first and second halves of the BB season have been found and are summarized in Table 3.

In the first half of the BB season, under predominant African influence, seasonally averaged BB tracer concentrations of $M_{BC_e} = 0.36 \pm 0.12\,\mu g\,m^{-3}$ and $c_{CO} = 140 \pm 30$ ppb were observed, whereas in the second half under predominant South American influence, $M_{BC_e} = 0.41 \pm 0.17\,\mu g\,m^{-3}$ and $c_{CO} = 190 \pm 70$ ppb were somewhat higher. The CCN concentrations increase throughout the dry season, with $N_{CCN,0.5} = 1100 \pm 500\,cm^{-3}$ in the African-BB and $N_{CCN,0.5} = 1800 \pm 900\,cm^{-3}$ in the South American-BB dominated states. In both periods, the BB-derived aerosol particles show high CCN efficiency, with 83 % and 87 % of particle activation at $S = 0.5$ % during the first and second halves of the BB season, respectively. Clearer differences between the two BB properties in the dry season were observed, however, for the SSA and the BC enhancement ratio, EnR_{BC} (Fig. 12 and Table 3). The aerosol was strongly absorbing in August, with a minimum SSA of about 0.85 ± 0.02. Subsequently, the absorption properties decreased towards November with a relative maximum in SSA at about 0.90 ± 0.03. These results are consistent with the large $\Delta N_{rBC}/\Delta N_{CN,20}$ of ∼ 40 % in the African UPL vs. the rather low $\Delta N_{rBC}/\Delta N_{CN,20}$ of ∼ 5 % in an exemplary Amazonian BB plume (Sect. 3.1, Fig. 5a). Moreover, Saturno et al. (2018b) have shown that the brown carbon (BrC) contribution to total absorption becomes increasingly important towards the end of the dry season. This is a further indication of the predominance of regional fires towards the later BB season, given that BrC is quickly photodegraded in the atmosphere after emission, with a typical lifetime of a few days to weeks (Fleming et al., 2020; Wong et al., 2019), comparable to the transport times of African BB emissions across the Atlantic.

In the Amazonian dry season, the EnR_{BC} values span from 3 to 14 $ng\,m^{-3}\,ppb^{-1}$ (daily values), with the highest values occurring under the influence of African plumes and associated with lower SSA (see also Saturno et al., 2018b). The EnR_{BC} decreases from its peak of $11 \pm 6\,ng\,m^{-3}\,ppb^{-1}$ in July–September to a relative minimum of $6 \pm 4\,ng\,m^{-3}\,ppb^{-1}$ around November (Fig. 12g). The high EnR_{BC} in African plumes can be attributed to more flaming combustion in the comparatively dry grassland, savanna, and shrubland vegetation, in contrast to more smoldering combustion of Amazonian deforestation fires in the moist tropical forests. For comparison, Darbyshire et al. (2019) reported, from the SAMBBA aircraft campaign over the southern Amazon Basin, EnR_{BC} of $3\,ng\,m^{-3}\,ppb^{-1}$ in the west associated with more smoldering combustion of pasture and forested areas, in contrast to EnR_{BC} of $12\,ng\,m^{-3}\,ppb^{-1}$ in the eastern part influenced by cerrado fires. Note that differences between ground-based (this section) and aircraft (Sect. 3.1) EnR_{BC} presented in this paper are due to removal processes, combustion phase, and, possibly, the use of different measurement techniques. However, the independent ground-based observations do show a clear decrease in EnR_{BC} from African- to Amazonian-BB dominated states, which is consistent with the aircraft measurements.

4 Summary and conclusions

In this study, we probed an event of African BB being advected into the Amazon Basin with a comprehensive set of instruments for aerosol and trace gas measurements onboard the HALO aircraft during the ACRIDICON-CHUVA campaign in September 2014. Vertical profiles over the Atlantic Ocean and inshore over the northeastern Amazon Basin revealed a horizontally extended rBC-enriched layer (referred to as the UPL) of about 300 m thickness at ~ 3.5 km altitude, which showed strongly elevated aerosol and trace gas concentrations compared to the other atmospheric levels below 6 km. The plume was dominated by aerosol particles in the accumulation-mode size range ($N_{acc} = 850 \pm 330\,cm^{-3}$), peaking at ~ 130 nm diameter, and consisting mostly of particles containing non-volatile material. Remarkably, rBC particles appeared to be a dominant species, with mean number and mass concentrations of $N_{rBC} = 280 \pm 110\,cm^{-3}$ and $M_{rBC} = 1.0 \pm 0.4\,\mu g\,m^{-3}$, respectively. This accounts for $\sim 40\,\%$ of the total aerosol number and 15 % of the submicrometer aerosol mass concentrations. The UPL also shows high mass fractions of organics (50 %), sulfate (17 %), ammonium (8 %), and nitrate (10 %). Along with rBC, high c_{CO} (150 ± 30 ppb) indicated that the layer originated from biomass burning. Moreover, the advanced photochemical aging of the plume was indicated by the elevated c_{O_3} (56 ± 9 ppb) and by the very high f_{44} measured by the AMS. Despite the large fraction of rBC, the aerosol in the UPL appeared to be very CCN efficient due to internal mixing of rBC with sulfate, nitrate, and oxygenated organic aerosol, with $\sim 70\,\%$ of particles activated at $S = 0.5\,\%$.

Backward trajectory analysis and remote sensing observations showed that the layer originated from BB in African grasslands, savannas, and shrublands. Therefore, the aerosol in the pollution layer upon arrival in South America, as probed by aircraft, has experienced at least 10 d of atmospheric aging over the African continent and the Atlantic Ocean. Moreover, multi-year remote sensing observations showed that layered atmospheric structures, and also the westward advection of African BB plumes, are a rather common phenomenon over the South Atlantic during the Amazonian dry season, peaking each year in August and September. Near the African coast, the vertical extent of the layer is a few kilometers, and it narrows down to only a few hundred meters while transported to South America. Based on the remote sensing data, we further calculate the DRF-TOA exerted by the pollution layer as a function of longitude. We found that the aging of the plume leads to a change in the DRF-TOA from a positive (warming) to a negative (cooling) effect as it moves westwards over the Atlantic. While the layered structure prevails all the way across the Atlantic for several days, it becomes quickly mixed vertically just a few hundreds of kilometers after reaching the South American continent. The aerosol particles in the layer are subsequently entrained into the continental boundary layer by convection and large-scale subsidence. We propose that long-range transport of such layers is the main pathway supplying African CCN and highly aged BC into the Amazonian atmosphere.

Long-term (2013–2018) ground-based aerosol measurements at the ATTO site in central Amazonia have demonstrated that long-range transported BB from Africa has a pronounced impact on aerosol particle properties within the dry season. From July to December, the Amazonian atmosphere is strongly influenced by BB aerosols, with corresponding increases in scattering and absorption coefficients (Saturno et al., 2018b; Rizzo et al., 2013), as well as the BB tracers, BC and CO. The interplay of African vs. South American BB emissions at ATTO is expressed by defined seasonal cycles of SSA, which increased from 0.85 in August to 0.90 in November, while EnR_{BC} decreased from 11 ± 6 to $6 \pm 4\,ng\,m^{-3}\,ppb^{-1}$.

This study highlights the importance of the transatlantic transport as a source of highly aged rBC and CCN-active particles to the Amazonian atmosphere, especially the northeastern regions, which are less impacted by anthropogenic pollution and regional fires. This process clearly merits future modeling investigations to assess its effects on regional radiative forcing as well as cloud properties and lifecycle.

Appendix A: List of frequently used symbols and acronyms

Description	Acronym
Aerosol optical depth	AOD
Aerosol Robotic Network	AERONET
Aerosol, Cloud, Precipitation, And Radiation Interactions And Dynamics Of Convective Cloud Systems Campaign	ACRIDICON-CHUVA
Amazon Tall Tower Observatory	ATTO
Atmospheric Infrared Sounder	AIRS
Backward trajectory	BT
Basic HALO Measurement And Sensor System	BAHAMAS
Biomass burning	BB
Black carbon	BC
Clean layer	CL
Cloud condensation nuclei	CCN
Cloud-Aerosol Lidar And Infrared Pathfinder Satellite Observations	CALIPSO
Condensation particle counters	CPC
Coordinated Universal Time	UTC
Compact Time-of-Flight Aerosol Mass Spectrometer	C-ToF-AMS
Fire radiative power	FRP
Long-range transport	LRT
Lower pollution layer	LPL
Marine boundary layer	MBL
Mass Absorption Aerosol Photometer	MAAP
Moderate Resolution Imaging Spectroradiometer	MODIS
Particle number size distributions	PNSD
Refractory black carbon	rBC
Region of interest	ROI
Single Particle Soot Photometer	SP2
Single scattering albedo	SSA
Ultra High Sensitivity Aerosol Spectrometer	UHSAS
Upper pollution layer	UPL

Data availability. The data of the key results presented here have been deposited in associated data files for use in follow-up studies. The HALO aircraft data (named "HALO.dat") and the ATTO data (named "ATTO.dat") used in this study are available in NASA Ames format under https://doi.org/10.17617/3.3r (Holanda et al., 2020a). Additional aircraft data from the ACRIDICON-CHUVA campaign can be found on the HALO database under https://halo-db.pa.op.dlr.de/ (DLR, 2020). Additional ATTO data can be found in the ATTO data portal under https://www.attodata.org/ (ATTO, 2020). The time series with cumulative fire count along backward trajectories (see Sect. 2.6) are available in NASA Ames format (named "H1000_Cer_Rain.dat") under https://doi.org/10.17617/3.3q (Holanda et al., 2020b). For data requests beyond the available data, please refer to the corresponding authors.

Supplement. The supplement related to this article is available online at: https://doi.org/10.5194/acp-20-4757-2020-supplement.

Author contributions. BAH conducted most of the data analysis and wrote the paper. CP, MOA, and UP supervised the work. MAF, QW, TD, JWK, CK, NM, HP, JS, CS, DW, and MW contributed specific parts of the data analysis. MLP, MD, TK, DF, LATM, DS, HS, JS, CS, BW, AW, MW, SB, HZ, MZ, CP, UP, and MOA conducted the measurements during the ACRIDICON-CHUVA campaign. BAH, MLP, JSa MS, FD, OOK, JB, MAF, FGM, JVL, and CP conducted the measurements at the ATTO site. JD, PA, HMJB, LATM, RB, YC, JWK, OOK, JM, and HSu contributed to the data analysis and interpretation through fruitful discussions and by providing valuable comments and ideas. All the authors contributed to the interpretation of the results and writing of the paper.

Competing interests. The authors declare that they have no conflict of interest.

Disclaimer. This paper contains results of research conducted under the Technical/Scientific Cooperation Agreement between the National Institute for Amazonian Research, the State University of Amazonas, and the Max-Planck-Gesellschaft e.V.; the opinions expressed are the entire responsibility of the authors and not of the participating institutions.

Special issue statement. This article is part of the special issue "Amazon Tall Tower Observatory (ATTO) Special Issue". It is not associated with a conference.

Acknowledgements. We recognize the Max Planck Society, the Conselho Nacional de Desenvolvimento Científico e Tecnológico (CNPq, Brazil), and the Max Planck Graduate Center with the Johannes Gutenberg University Mainz (MPGC) for the financial support. We thank the entire ACRIDICON-CHUVA team for the fruitful scientific cooperation. Special thanks goes to the HALO pilots, Steffen Gemsa, Michael Grossrubatscher, and Stefan Grillenbeck. We thank Volker Dreiling, the Sensor and Data Team of DLR Flight Experiments, and the HALO team of the DLR for their cooperation. We acknowledge the generous support of the ACRIDICON-CHUVA campaign by the Max Planck Society, the German Aerospace Center (DLR), FAPESP (São Paulo Research Foundation), and the German Science Foundation (Deutsche Forschungsgemeinschaft, DFG) within the DFG Priority Program "Atmospheric and Earth System Research with the Research Aircraft HALO (High Altitude and Long Range Research Aircraft)". Bernadett Weinzierl, Maximilian Dollner, and Adrian Walser would like to acknowledge funding from the European Research Council under the European Community's Horizon 2020 research and innovation framework program/ERC grant agreement 640458 (A-LIFE). Paulo Artaxo acknowledges FAPESP (Fundação de Amparo à Pesquisa do Estado de São Paulo) grant 2017/17047-0. Marco A. Franco acknowledges the scholarship from CNPq, project 169842/2017-7, for supporting his PhD studies at the University of São Paulo, São Paulo, Brazil, and CAPES, project 88887.368025/2019-00, for supporting 6 months of a sandwich doctorate program at the Max Planck Institute for Chemisty, Mainz, Germany. For the operation of the ATTO site, we acknowledge the support by the Max Planck Society, the German Federal Ministry of Education and Research and the Brazilian Ministério da Ciência, Tecnologia e Inovação as well as the Amazon State University (UEA), FAPEAM, LBA/INPA, and SDS/CEUC/RDS-Uatumã. Special thanks for all the people involved in ATTO project, in particular Susan Trumbore, Carlos Alberto Quesada, Reiner Ditz, Stefan Wolff, Jürgen Kesselmeier, Antonio O. Manzi, Andrew Crozier, Thomas Disper, Alcides Camargo Ribeiro, Hermes Braga Xavier, Nagib Alberto de Castro Souza, Adir Vasconcelos Brandão, Amauri Rodriguês Perreira, Antonio Huxley Melo Nascimento, André Luiz Matos, Delano Campos, Fábio Jorge, Roberta Pereira de Souza, Bruno Takeshi, Wallace Rabelo Costa, Uwe Schultz, Karl Kübler, Olaf Kolle, Martin Hertel, Kerstin Hippler, and Steffen Schmidt. Remote sensing analyses and visualizations used in this study were produced with the Giovanni online data system, developed and maintained by the NASA GES DISC. We acknowledge the National Oceanic and Atmospheric Administration (NOAA) Air Resources Laboratory (ARL) for the HYSPLIT transport and dispersion model. We thank Arthur J. Sedlacek, Daniel Moran-Zuloaga, Maria Praß, Leslie Kremper, Tobias Könemann, Jan-David Förster, Björn Nillius, Anywhere Tsokankunku, and Oliver Lauer for their support and inspiring discussions.

Financial support. This research has been supported by the Max Planck Society, the Max Planck Graduate Center with the Johannes Gutenberg University Mainz (MPGC), the Bundesministerium für Bildung und Forschung (BMBF contracts 01LB1001A, 01LK1602A, 01LK1602B, and 01LG1205E), the Brazilian Ministério da Ciência, Tecnologia e Inovação (MCTI/FINEP contract 01.11.01248.00), the Conselho Nacional de Desenvolvimento Científico e Tecnológico (CNPq, Brazil) (process 200723/2015-4), the FAPESP (Fundação de Amparo à Pesquisa do Estado de São Paulo) (grant no. 2017/17047-0), the CNPq project (grant no. 169842/2017-7), the CAPES project (grant no. 88887.368025/2019-00), and the European Commission, H2020

Research Infrastructures (A-LIFE (grant no. 640458)). This study was also supported by EU Project HAIC under FP7-AAT-2012-3.5.1-1 and by the German Science Foundation within DFG SPP 1294 HALO by contract nos. VO1504/4-1, JU 3059/1-1 and SCHN1138/1-2.

The article processing charges for this open-access publication were covered by the Max Planck Society.

Review statement. This paper was edited by Gilberto Fisch and reviewed by two anonymous referees.

References

Adachi, K., Sedlacek, A. J., Kleinman, L., Chand, D., Hubbe, J. M., and Buseck, P. R.: Volume changes upon heating of aerosol particles from biomass burning using transmission electron microscopy, Aerosol Sci. Tech., 52, 46–56, https://doi.org/10.1080/02786826.2017.1373181, 2018.

Adebiyi, A. A. and Zuidema, P.: The role of the southern African easterly jet in modifying the southeast Atlantic aerosol and cloud environments, Q. J. Roy. Meteor. Soc., 142, 1574–1589, https://doi.org/10.1002/qj.2765, 2016.

Allen, A. G. and Miguel, A. H.: Biomass Burning in the Amazon: Characterization of the Ionic Component of Aerosols Generated from Flaming and Smoldering Rainforest and Savannah, Environ. Sci. Technol., 29, 486–493, https://doi.org/10.1021/es00002a026, 1995.

Andela, N. and van der Werf, G. R.: Recent trends in African fires driven by cropland expansion and El Niño to La Niña transition, Nat. Clim. Change, 4, 791–795, https://doi.org/10.1038/nclimate2313, 2014.

Anderson, G. P., Clough, S. A., Kneizys, F. X., Chetwynd, J. H., and Shettle, E. P.: AFGL (Air Force Geophysical Laboratory) atmospheric constituent profiles (0.120 km), Environmental research papers, USA, 1986.

Andreae, M. O.: Biomass burning: Its history, use and distribution and its impact on environmental quality and global climate, in: Global Biomass Burning: Atmospheric, Climatic and Biospheric Implications, edited by: Levine, J. S., 3–21, MIT Press, Cambridge, Mass., USA, 1991.

Andreae, M. O.: Emission of trace gases and aerosols from biomass burning – an updated assessment, Atmos. Chem. Phys., 19, 8523–8546, https://doi.org/10.5194/acp-19-8523-2019, 2019.

Andreae, M. O. and Gelencsér, A.: Black carbon or brown carbon? The nature of light-absorbing carbonaceous aerosols, Atmos. Chem. Phys., 6, 3131–3148, https://doi.org/10.5194/acp-6-3131-2006, 2006.

Andreae, M. O. and Merlet, P.: Emission of trace gases and aerosols from biomass burning, Global Biogeochem. Cy., 15, 955–966, https://doi.org/10.1029/2000GB001382, 2001.

Andreae, M. O. and Ramanathan, V.: Climate's Dark Forcings, Science, 340, 280–281, https://doi.org/10.1126/science.1235731, 2013.

Andreae, M. O., Browell, E. V., Garstang, M., Gregory, G. L., Harriss, R. C., Hill, G. F., Jacob, D. J., Pereira, M. C., Sachse, G. W., Setzer, A. W., Dias, P. L. S., Talbot, R. W., Torres, A. L., and Wofsy, S. C.: Biomass-burning emissions and associated haze layers over Amazonia, J. Geophys. Res., 93, 1509, https://doi.org/10.1029/JD093iD02p01509, 1988.

Andreae, M. O., Anderson, B. E., Blake, D. R., Bradshaw, J. D., Collins, J. E., Gregory, G. L., Sachse, G. W., and Shipham, M. C.: Influence of plumes from biomass burning on atmospheric chemistry over the equatorial and tropical South Atlantic during CITE 3, J. Geophys. Res., 99, 12793, https://doi.org/10.1029/94JD00263, 1994.

Andreae, M. O., Artaxo, P., Beck, V., Bela, M., Freitas, S., Gerbig, C., Longo, K., Munger, J. W., Wiedemann, K. T., and Wofsy, S. C.: Carbon monoxide and related trace gases and aerosols over the Amazon Basin during the wet and dry seasons, Atmos. Chem. Phys., 12, 6041–6065, https://doi.org/10.5194/acp-12-6041-2012, 2012.

Andreae, M. O., Acevedo, O. C., Araùjo, A., Artaxo, P., Barbosa, C. G. G., Barbosa, H. M. J., Brito, J., Carbone, S., Chi, X., Cintra, B. B. L., da Silva, N. F., Dias, N. L., Dias-Júnior, C. Q., Ditas, F., Ditz, R., Godoi, A. F. L., Godoi, R. H. M., Heimann, M., Hoffmann, T., Kesselmeier, J., Könemann, T., Krüger, M. L., Lavric, J. V., Manzi, A. O., Lopes, A. P., Martins, D. L., Mikhailov, E. F., Moran-Zuloaga, D., Nelson, B. W., Nölscher, A. C., Santos Nogueira, D., Piedade, M. T. F., Pöhlker, C., Pöschl, U., Quesada, C. A., Rizzo, L. V., Ro, C.-U., Ruckteschler, N., Sá, L. D. A., de Oliveira Sá, M., Sales, C. B., dos Santos, R. M. N., Saturno, J., Schöngart, J., Sörgel, M., de Souza, C. M., de Souza, R. A. F., Su, H., Targhetta, N., Tóta, J., Trebs, I., Trumbore, S., van Eijck, A., Walter, D., Wang, Z., Weber, B., Williams, J., Winderlich, J., Wittmann, F., Wolff, S., and Yáñez-Serrano, A. M.: The Amazon Tall Tower Observatory (ATTO): overview of pilot measurements on ecosystem ecology, meteorology, trace gases, and aerosols, Atmos. Chem. Phys., 15, 10723–10776, https://doi.org/10.5194/acp-15-10723-2015, 2015.

Andreae, M. O., Afchine, A., Albrecht, R., Holanda, B. A., Artaxo, P., Barbosa, H. M. J., Borrmann, S., Cecchini, M. A., Costa, A., Dollner, M., Fütterer, D., Järvinen, E., Jurkat, T., Klimach, T., Konemann, T., Knote, C., Krämer, M., Krisna, T., Machado, L. A. T., Mertes, S., Minikin, A., Pöhlker, C., Pöhlker, M. L., Pöschl, U., Rosenfeld, D., Sauer, D., Schlager, H., Schnaiter, M., Schneider, J., Schulz, C., Spanu, A., Sperling, V. B., Voigt, C., Walser, A., Wang, J., Weinzierl, B., Wendisch, M., and Ziereis, H.: Aerosol characteristics and particle production in the upper troposphere over the Amazon Basin, Atmos. Chem. Phys., 18, 921–961, https://doi.org/10.5194/acp-18-921-2018, 2018.

Anselmo, E. M., Shumacher, C., and Machado, L. A. T.: The Amazonian Low-level Jet and its Connection to Convective Cloud Propagation and Evolution, Mon. Weather Rev., submitted, 2020.

Ansmann, A., Baars, H., Tesche, M., Müller, D., Althausen, D., Engelmann, R., Pauliquevis, T., and Artaxo, P.: Dust and smoke transport from Africa to South America: Lidar profiling over Cape Verde and the Amazon rainforest, Geophys. Res. Lett., 36, L11802, https://doi.org/10.1029/2009GL037923, 2009.

Artaxo, P., Rizzo, L. V., Brito, J. F., Barbosa, H. M. J., Arana, A., Sena, E. T., Cirino, G. G., Bastos, W., Martin, S. T., and Andreae, M. O.: Atmospheric aerosols in Amazonia and land use change: from natural biogenic to biomass burning conditions, Faraday Discuss., 165, 203, https://doi.org/10.1039/c3fd00052d, 2013.

ATTO: ATTO data portal, available at: https://www.attodata.org/, last access: 17 April 2020.

Baars, H., Ansmann, A., Althausen, D., Engelmann, R., Artaxo, P., Pauliquevis, T., and Souza, R.: Further evidence for significant smoke transport from Africa to Amazonia, Geophys. Res. Lett., 38, L20802, https://doi.org/10.1029/2011GL049200, 2011.

Baehr, J.: Aircraft observations of NO, NO_y , CO, and O_3 in the upper troposphere from 60° N to 60° S – Interhemispheric differences at mitlatitudes, Geophys. Res. Lett., 30, 1598, https://doi.org/10.1029/2003GL016935, 2003.

Barbosa, P. M., Stroppiana, D., Grégoire, J.-M., and Cardoso Pereira, J. M.: An assessment of vegetation fire in Africa (1981–1991): Burned areas, burned biomass, and atmospheric emissions, Global Biogeochem. Cy., 13, 933–950, https://doi.org/10.1029/1999GB900042, 1999.

Barkley, A. E., Prospero, J. M., Mahowald, N., Hamilton, D. S., Popendorf, K. J., Oehlert, A. M., Pourmand, A., Gatineau, A., Panechou-Pulcherie, K., Blackwelder, P., and Gaston, C. J.: African biomass burning is a substantial source of phosphorus deposition to the Amazon, Tropical Atlantic Ocean, and Southern Ocean, P. Natl. Acad. Sci., 116, 16216–16221, https://doi.org/10.1073/pnas.1906091116, 2019.

Bond, T. C., Doherty, S. J., Fahey, D. W., Forster, P. M., Berntsen, T., Deangelo, B. J., Flanner, M. G., Ghan, S., Kärcher, B., Koch, D., Kinne, S., Kondo, Y., Quinn, P. K., Sarofim, M. C., Schultz, M. G., Schulz, M., Venkataraman, C., Zhang, H., Zhang, S., Bellouin, N., Guttikunda, S. K., Hopke, P. K., Jacobson, M. Z., Kaiser, J. W., Klimont, Z., Lohmann, U., Schwarz, J. P., Shindell, D., Storelvmo, T., Warren, S. G., and Zender, C. S.: Bounding the role of black carbon in the climate system: A scientific assessment, J. Geophys. Res.-Atmos., 118, 5380–5552, https://doi.org/10.1002/jgrd.50171, 2013.

Boucher, O., Randall, D., Artaxo, P., Bretherton, C., Feingold, G., Forster, P., Kerminen, V.-M., Kondo, Y., Liao, H., Lohmann, U., Rasch, P., Satheesh, S. K., Sherwood, S., Stevens, B., and Zhang, X. Y.: Clouds and Aerosols, in: Climate Change 2013: The Physical Science Basis. Contribution of Working Group I to the Fifth Assessment Report of the Intergovernmental Panel on Climate Change, edited by: Stocker, T. F., Qin, D., Plattner, G.-K., Tignor, M., Allen, S. K., Boschung, J., Nauels, A., Xia, Y., Bex, V., and Midgley, P. M., Cambridge University Press, Cambridge, UK and New York, NY, USA, 2013.

Boucher, O., Balkanski, Y., Hodnebrog, Ø., Myhre, C. L., Myhre, G., Quaas, J., Samset, B. H., Schutgens, N., Stier, P., and Wang, R.: Jury is still out on the radiative forcing by black carbon, P. Natl. Acad. Sci. USA, 113, E5092–E5093, https://doi.org/10.1073/pnas.1607005113, 2016.

Bozem, H., Fischer, H., Gurk, C., Schiller, C. L., Parchatka, U., Koenigstedt, R., Stickler, A., Martinez, M., Harder, H., Kubistin, D., Williams, J., Eerdekens, G., and Lelieveld, J.: Influence of corona discharge on the ozone budget in the tropical free troposphere: a case study of deep convection during GABRIEL, Atmos. Chem. Phys., 14, 8917–8931, https://doi.org/10.5194/acp-14-8917-2014, 2014.

Brioude, J., Cooper, O. R., Feingold, G., Trainer, M., Freitas, S. R., Kowal, D., Ayers, J. K., Prins, E., Minnis, P., McKeen, S. A., Frost, G. J., and Hsie, E.-Y.: Effect of biomass burning on marine stratocumulus clouds off the California coast, Atmos. Chem. Phys., 9, 8841–8856, https://doi.org/10.5194/acp-9-8841-2009, 2009.

Brito, J., Rizzo, L. V., Morgan, W. T., Coe, H., Johnson, B., Haywood, J., Longo, K., Freitas, S., Andreae, M. O., and Artaxo, P.: Ground-based aerosol characterization during the South American Biomass Burning Analysis (SAMBBA) field experiment, Atmos. Chem. Phys., 14, 12069–12083, https://doi.org/10.5194/acp-14-12069-2014, 2014.

Cai, Y., Montague, D. C., Mooiweer-Bryan, W., and Deshler, T.: Performance characteristics of the ultra high sensitivity aerosol spectrometer for particles between 55 and 800 nm: Laboratory and field studies, J. Aerosol Sci., 39, 759–769, https://doi.org/10.1016/j.jaerosci.2008.04.007, 2008.

Chen, Q., Farmer, D. K., Rizzo, L. V., Pauliquevis, T., Kuwata, M., Karl, T. G., Guenther, A., Allan, J. D., Coe, H., Andreae, M. O., Pöschl, U., Jimenez, J. L., Artaxo, P., and Martin, S. T.: Submicron particle mass concentrations and sources in the Amazonian wet season (AMAZE-08), Atmos. Chem. Phys., 15, 3687–3701, https://doi.org/10.5194/acp-15-3687-2015, 2015.

Cheng, T., Wu, Y., and Chen, H.: Effects of morphology on the radiative properties of internally mixed light absorbing carbon aerosols with different aging status, Opt. Express, 22, 15904, https://doi.org/10.1364/OE.22.015904, 2014.

Clarke, A. D.: A thermo-optic technique for in situ analysis of size-resolved aerosol physicochemistry, Atmos. Environ. A-Gen., 25, 635–644, https://doi.org/10.1016/0960-1686(91)90061-B, 1991.

Colarco, P., Silva, A., Chin, M., and Diehl, T.: Online simulations of global aerosol distributions in the NASA GEOS 4 model and comparisons to satellite and ground – based aerosol optical depth, J. Geophys. Res.-Atmos., 115, D14207, https://doi.org/10.1029/2009JD012820, 2010.

Cubison, M. J., Ortega, A. M., Hayes, P. L., Farmer, D. K., Day, D., Lechner, M. J., Brune, W. H., Apel, E., Diskin, G. S., Fisher, J. A., Fuelberg, H. E., Hecobian, A., Knapp, D. J., Mikoviny, T., Riemer, D., Sachse, G. W., Sessions, W., Weber, R. J., Weinheimer, A. J., Wisthaler, A., and Jimenez, J. L.: Effects of aging on organic aerosol from open biomass burning smoke in aircraft and laboratory studies, Atmos. Chem. Phys., 11, 12049–12064, https://doi.org/10.5194/acp-11-12049-2011, 2011.

Dajuma, A., Ogunjobi, K. O., Vogel, H., Knippertz, P., Silué, S., N'Datchoh, E. T., Yoboué, V., and Vogel, B.: Cloud-venting induced downward mixing of the Central African biomass burning plume during the West Africa summer monsoon, Atmos. Chem. Phys. Discuss., https://doi.org/10.5194/acp-2019-617, in review, 2019.

Darbyshire, E., Morgan, W. T., Allan, J. D., Liu, D., Flynn, M. J., Dorsey, J. R., O'Shea, S. J., Lowe, D., Szpek, K., Marenco, F., Johnson, B. T., Bauguitte, S., Haywood, J. M., Brito, J. F., Artaxo, P., Longo, K. M., and Coe, H.: The vertical distribution of biomass burning pollution over tropical South America from aircraft in situ measurements during SAMBBA, Atmos. Chem. Phys., 19, 5771–5790, https://doi.org/10.5194/acp-19-5771-2019, 2019.

Das, S., Harshvardhan, H., Bian, H., Chin, M., Curci, G., Protonotariou, A. P., Mielonen, T., Zhang, K., Wang, H., and Liu, X.: Biomass burning aerosol transport and vertical distribution over the South African-Atlantic region, J. Geophys. Res.-Atmos., 122, 6391–6415, https://doi.org/10.1002/2016JD026421, 2017.

Denjean, C., Bourrianne, T., Burnet, F., Mallet, M., Maury, N., Colomb, A., Dominutti, P., Brito, J., Dupuy, R., Sellegri, K., Schwarzenboeck, A., Flamant, C., and Knippertz, P.: Light ab-

sorption properties of aerosols over Southern West Africa, Atmos. Chem. Phys. Discuss., https://doi.org/10.5194/acp-2019-587, in review, 2019.

de Sá, S. S., Rizzo, L. V., Palm, B. B., Campuzano-Jost, P., Day, D. A., Yee, L. D., Wernis, R., Isaacman-VanWertz, G., Brito, J., Carbone, S., Liu, Y. J., Sedlacek, A., Springston, S., Goldstein, A. H., Barbosa, H. M. J., Alexander, M. L., Artaxo, P., Jimenez, J. L., and Martin, S. T.: Contributions of biomass-burning, urban, and biogenic emissions to the concentrations and light-absorbing properties of particulate matter in central Amazonia during the dry season, Atmos. Chem. Phys., 19, 7973–8001, https://doi.org/10.5194/acp-19-7973-2019, 2019.

Diab, R. D., Thompson, A. M., Zunckel, M., Coetzee, G. J. R., Combrink, J., Bodeker, G. E., Fishman, J., Sokolic, F., McNamara, D. P., Archer, C. B., and Nganga, D.: Vertical ozone distribution over southern Africa and adjacent oceans during SAFARI-92, J. Geophys. Res.-Atmos., 101, 23823–23833, https://doi.org/10.1029/96JD01267, 1996.

Ditas, J., Ma, N., Zhang, Y., Assmann, D., Neumaier, M., Riede, H., and Karu, E.: Strong impact of wildfires on the abundance and aging of black carbon in the lowermost stratosphere, P. Natl. Acad. Sci. USA, 115, E11595–E11603, https://doi.org/10.1073/pnas.1806868115, 2018.

DLR: Halo database, available at: https://halo-db.pa.op.dlr.de/, last access: 17 April 2020.

Drewnick, F., Hings, S. S., DeCarlo, P., Jayne, J. T., Gonin, M., Fuhrer, K., Weimer, S., Jimenez, J. L., Demerjian, K. L., Borrmann, S., and Worsnop, D. R.: A New Time-of-Flight Aerosol Mass Spectrometer (TOF-AMS)–Instrument Description and First Field Deployment, Aerosol Sci. Tech., 39, 637–658, https://doi.org/10.1080/02786820500182040, 2005.

Earl, N., Simmonds, I., and Tapper, N.: Weekly cycles of global fires-Associations with religion, wealth and culture, and insights into anthropogenic influences on global climate, Geophys. Res. Lett., 42, 9579–9589, https://doi.org/10.1002/2015GL066383, 2015.

Emde, C., Buras-Schnell, R., Kylling, A., Mayer, B., Gasteiger, J., Hamann, U., Kylling, J., Richter, B., Pause, C., Dowling, T., and Bugliaro, L.: The libRadtran software package for radiative transfer calculations (version 2.0.1), Geosci. Model Dev., 9, 1647–1672, https://doi.org/10.5194/gmd-9-1647-2016, 2016.

Evans, K. F.: The Spherical Harmonics Discrete Ordinate Method for Three-Dimensional Atmospheric Radiative Transfer, J. Atmos. Sci., 55, 429–446, https://doi.org/10.1175/1520-0469(1998)055<0429:TSHDOM>2.0.CO;2, 1998.

Flamant, C., Knippertz, P., Fink, A. H., Akpo, A., Brooks, B., Chiu, C. J., Coe, H., Danuor, S., Evans, M., Jegede, O., Kalthoff, N., Konaré, A., Liousse, C., Lohou, F., Mari, C., Schlager, H., Schwarzenboeck, A., Adler, B., Amekudzi, L., Aryee, J., Ayoola, M., Batenburg, A. M., Bessardon, G., Borrmann, S., Brito, J., Bower, K., Burnet, F., Catoire, V., Colomb, A., Denjean, C., Fosu-Amankwah, K., Hill, P. G., Lee, J., Lothon, M., Maranan, M., Marsham, J., Meynadier, R., Ngamini, J.-B., Rosenberg, P., Sauer, D., Smith, V., Stratmann, G., Taylor, J. W., Voigt, C., and Yoboué, V.: The Dynamics–Aerosol–Chemistry–Cloud Interactions in West Africa Field Campaign: Overview and Research Highlights, B. Am. Meteorol. Soc., 99, 83–104, https://doi.org/10.1175/BAMS-D-16-0256.1, 2018.

Fleming, L. T., Lin, P., Roberts, J. M., Selimovic, V., Yokelson, R., Laskin, J., Laskin, A., and Nizkorodov, S. A.: Molecular composition and photochemical lifetimes of brown carbon chromophores in biomass burning organic aerosol, Atmos. Chem. Phys., 20, 1105–1129, https://doi.org/10.5194/acp-20-1105-2020, 2020.

Fuller, K. A., Malm, W. C., and Kreidenweis, S. M.: Effects of mixing on extinction by carbonaceous particles, J. Geophys. Res.-Atmos., 104, 15941–15954, https://doi.org/10.1029/1998JD100069, 1999.

Fuzzi, S., Andreae, M. O., Huebert, B. J., Kulmala, M., Bond, T. C., Boy, M., Doherty, S. J., Guenther, A., Kanakidou, M., Kawamura, K., Kerminen, V.-M., Lohmann, U., Russell, L. M., and Pöschl, U.: Critical assessment of the current state of scientific knowledge, terminology, and research needs concerning the role of organic aerosols in the atmosphere, climate, and global change, Atmos. Chem. Phys., 6, 2017–2038, https://doi.org/10.5194/acp-6-2017-2006, 2006.

Gerbig, C., Schmitgen, S., Kley, D., Volz-Thomas, A., Dewey, K., and Haaks, D.: An improved fast-response vacuum-UV resonance fluorescence CO instrument, J. Geophys. Res.-Atmos., 104, 1699–1704, https://doi.org/10.1029/1998JD100031, 1999.

Grieshop, A. P., Logue, J. M., Donahue, N. M., and Robinson, A. L.: Laboratory investigation of photochemical oxidation of organic aerosol from wood fires 1: measurement and simulation of organic aerosol evolution, Atmos. Chem. Phys., 9, 1263–1277, https://doi.org/10.5194/acp-9-1263-2009, 2009.

Gueymard, C. A.: The sun's total and spectral irradiance for solar energy applications and solar radiation models, Sol. Energy, 76, 423–453, https://doi.org/10.1016/j.solener.2003.08.039, 2004.

Guyon, P., Frank, G. P., Welling, M., Chand, D., Artaxo, P., Rizzo, L., Nishioka, G., Kolle, O., Fritsch, H., Silva Dias, M. A. F., Gatti, L. V., Cordova, A. M., and Andreae, M. O.: Airborne measurements of trace gas and aerosol particle emissions from biomass burning in Amazonia, Atmos. Chem. Phys., 5, 2989–3002, https://doi.org/10.5194/acp-5-2989-2005, 2005.

Hegg, D. A., Radke, L. F., and Hobbs, P. V.: Particle production associated with marine clouds, J. Geophys. Res., 95, 13917, https://doi.org/10.1029/JD095iD09p13917, 1990.

Heintzenberg, J.: Properties of the Log-Normal Particle Size Distribution, Aerosol Sci. Tech., 21, 46–48, https://doi.org/10.1080/02786829408959695, 1994.

Hobbs, P. V.: Clean air slots amid dense atmospheric pollution in southern Africa, J. Geophys. Res., 108, 1–8, https://doi.org/10.1029/2002JD002156, 2003.

Holanda, B., Pöhlker, C., Pöhlker, M., and Lavrič, J.: ATTO and HALO data related to Holanda et al 2020, Max Planck Society, https://doi.org/10.17617/3.3r, 2020a.

Holanda, B., Pöhlker, C., and Walter, D.: Fire contact of ATTO backward trajectories, Max Planck Society, https://doi.org/10.17617/3.3q, 2020b.

Holben, B. N., Eck, T. F., Slutsker, I., Tanré, D., Buis, J. P., Setzer, A., Vermote, E., Reagan, J. A., Kaufman, Y. J., Nakajima, T., Lavenu, F., Jankowiak, I., and Smirnov, A.: AERONET – A Federated Instrument Network and Data Archive for Aerosol Characterization, Remote Sens. Environ., 66, 1–16, https://doi.org/10.1016/S0034-4257(98)00031-5, 1998.

Ichoku, C. and Ellison, L.: Global top-down smoke-aerosol emissions estimation using satellite fire radiative power

measurements, Atmos. Chem. Phys., 14, 6643–6667, https://doi.org/10.5194/acp-14-6643-2014, 2014.

IPCC: Climate Change 2013: The Physical Science Basis, Contribution of Working Group I to the Fifth Assessment Report of the Intergovernmental Panel on Climate Change, edited by: Stocker, T. F., Qin, D., Plattner, G.-K., Tignor, M., Allen, S. K., Boschung, J., Nauels, A., Xia, Y., Bex, V., and Midgley, P. M., Cambridge University Press, Cambridge, UK, New York, NY, USA, 1535 pp., 2013.

Isaacman-VanWertz, G., Massoli, P., O'Brien, R., Lim, C., Franklin, J. P., Moss, J. A., Hunter, J. F., Nowak, J. B., Canagaratna, M. R., Misztal, P. K., Arata, C., Roscioli, J. R., Herndon, S. T., Onasch, T. B., Lambe, A. T., Jayne, J. T., Su, L., Knopf, D. A., Goldstein, A. H., Worsnop, D. R., and Kroll, J. H.: Chemical evolution of atmospheric organic carbon over multiple generations of oxidation, Nat. Chem., 10, 462–468, https://doi.org/10.1038/s41557-018-0002-2, 2018.

Jen, C. N., Hatch, L. E., Selimovic, V., Yokelson, R. J., Weber, R., Fernandez, A. E., Kreisberg, N. M., Barsanti, K. C., and Goldstein, A. H.: Speciated and total emission factors of particulate organics from burning western US wildland fuels and their dependence on combustion efficiency, Atmos. Chem. Phys., 19, 1013–1026, https://doi.org/10.5194/acp-19-1013-2019, 2019.

Kaiser, J. W., Heil, A., Andreae, M. O., Benedetti, A., Chubarova, N., Jones, L., Morcrette, J.-J., Razinger, M., Schultz, M. G., Suttie, M., and van der Werf, G. R.: Biomass burning emissions estimated with a global fire assimilation system based on observed fire radiative power, Biogeosciences, 9, 527–554, https://doi.org/10.5194/bg-9-527-2012, 2012.

Kerminen, V.-M., Chen, X., Vakkari, V., Petäjä, T., Kulmala, M., and Bianchi, F.: Atmospheric new particle formation and growth: review of field observations, Environ. Res. Lett., 13, 103003, https://doi.org/10.1088/1748-9326/aadf3c, 2018.

Kirchhoff, V. W. J. H., Hilsenrath, E., Motta, A. G., Sahai, Y., and Medrano-B, R. A.: Equatorial ozone characteristics as measured at Natal (5.9° S, 35.2° W), J. Geophys. Res., 88, 6812, https://doi.org/10.1029/JC088iC11p06812, 1983.

Kirchhoff, V. W. J. H., Barnes, R. A., and Torres, A. L.: Ozone climatology at Natal, Brazil, from in situ ozonesonde data, J. Geophys. Res., 96, 10899, https://doi.org/10.1029/91JD01212, 1991.

Koch, D. and Del Genio, A. D.: Black carbon semi-direct effects on cloud cover: review and synthesis, Atmos. Chem. Phys., 10, 7685–7696, https://doi.org/10.5194/acp-10-7685-2010, 2010.

Konovalov, I. B., Beekmann, M., Berezin, E. V., Formenti, P., and Andreae, M. O.: Probing into the aging dynamics of biomass burning aerosol by using satellite measurements of aerosol optical depth and carbon monoxide, Atmos. Chem. Phys., 17, 4513–4537, https://doi.org/10.5194/acp-17-4513-2017, 2017.

Konovalov, I. B., Beekmann, M., Golovushkin, N. A., and Andreae, M. O.: Nonlinear behavior of organic aerosol in biomass burning plumes: a microphysical model analysis, Atmos. Chem. Phys., 19, 12091–12119, https://doi.org/10.5194/acp-19-12091-2019, 2019.

Krüger, M. L., Mertes, S., Klimach, T., Cheng, Y. F., Su, H., Schneider, J., Andreae, M. O., Pöschl, U., and Rose, D.: Assessment of cloud supersaturation by size-resolved aerosol particle and cloud condensation nuclei (CCN) measurements, Atmos. Meas. Tech., 7, 2615–2629, https://doi.org/10.5194/amt-7-2615-2014, 2014.

Laborde, M., Crippa, M., Tritscher, T., Jurányi, Z., Decarlo, P. F., Temime-Roussel, B., Marchand, N., Eckhardt, S., Stohl, A., Baltensperger, U., Prévôt, A. S. H., Weingartner, E., and Gysel, M.: Black carbon physical properties and mixing state in the European megacity Paris, Atmos. Chem. Phys., 13, 5831–5856, https://doi.org/10.5194/acp-13-5831-2013, 2013.

Lawson, D. R. and Winchester, J. W.: Sulfur, potassium, and phosphorus associations in aerosols from South American tropical rain forests, J. Geophys. Res., 84, 3723, https://doi.org/10.1029/JC084iC07p03723, 1979.

Levin, E. J. T., McMeeking, G. R., Carrico, C. M., Mack, L. E., Kreidenweis, S. M., Wold, C. E., Moosmüller, H., Arnott, W. P., Hao, W. M., Collett, J. L., and Malm, W. C.: Biomass burning smoke aerosol properties measured during Fire Laboratory at Missoula Experiments (FLAME), J. Geophys. Res., 115, D18210, https://doi.org/10.1029/2009JD013601, 2010.

Liu, D., Whitehead, J., Alfarra, M. R., Reyes-Villegas, E., Spracklen, D. V., Reddington, C. L., Kong, S., Williams, P. I., Ting, Y. C., Haslett, S., Taylor, J. W., Flynn, M. J., Morgan, W. T., McFiggans, G., Coe, H., and Allan, J. D.: Black-carbon absorption enhancement in the atmosphere determined by particle mixing state, Nat. Geosci., 10, 184–188, https://doi.org/10.1038/ngeo2901, 2017.

Logan, J. A. and Kirchhoff, V. W. J. H.: Seasonal variations of tropospheric ozone at Natal, Brazil, J. Geophys. Res.-Atmos., 91, 7875–7881, https://doi.org/10.1029/JD091iD07p07875, 1986.

Machado, L. A. T., Calheiros, A. J. P., Biscaro, T., Giangrande, S., Silva Dias, M. A. F., Cecchini, M. A., Albrecht, R., Andreae, M. O., Araujo, W. F., Artaxo, P., Borrmann, S., Braga, R., Burleyson, C., Eichholz, C. W., Fan, J., Feng, Z., Fisch, G. F., Jensen, M. P., Martin, S. T., Pöschl, U., Pöhlker, C., Pöhlker, M. L., Ribaud, J.-F., Rosenfeld, D., Saraiva, J. M. B., Schumacher, C., Thalman, R., Walter, D., and Wendisch, M.: Overview: Precipitation characteristics and sensitivities to environmental conditions during GoAmazon2014/5 and ACRIDICON-CHUVA, Atmos. Chem. Phys., 18, 6461–6482, https://doi.org/10.5194/acp-18-6461-2018, 2018.

Marenco, F., Johnson, B., Langridge, J. M., Mulcahy, J., Benedetti, A., Remy, S., Jones, L., Szpek, K., Haywood, J., Longo, K., and Artaxo, P.: On the vertical distribution of smoke in the Amazonian atmosphere during the dry season, Atmos. Chem. Phys., 16, 2155–2174, https://doi.org/10.5194/acp-16-2155-2016, 2016.

Martin, S. T., Andreae, M. O., Artaxo, P., Baumgardner, D., Chen, Q., Goldstein, A. H., Guenther, A., Heald, C. L., Mayol-Bracero, O. L., McMurry, P. H., Pauliquevis, T., Pöschl, U., Prather, K. A., Roberts, G. C., Saleska, S. R., Silva Dias, M. A., Spracklen, D. V., Swietlicki, E., and Trebs, I.: Sources and properties of Amazonian aerosol particles, Rev. Geophys., 48, RG2002, https://doi.org/10.1029/2008RG000280, 2010.

Martin, S. T., Artaxo, P., Machado, L., Manzi, A. O., Souza, R. A. F., Schumacher, C., Wang, J., Biscaro, T., Brito, J., Calheiros, A., Jardine, K., Medeiros, A., Portela, B., De Sá, S. S., Adachi, K., Aiken, A. C., Alblbrecht, R., Alexander, L., Andreae, M. O., Barbosa, H. M. J., Buseck, P., Chand, D., Comstmstmstock, J. M., Day, D. A., Dubey, M., Fan, J., Fastst, J., Fisch, G., Fortner, E., Giangrande, S., Gilllles, M., Goldststein, A. H., Guenther, A., Hubbe, J., Jensen, M., Jimenez, J. L., Keutstsch, F. N., Kim, S., Kuang, C., Laskskin, A., McKinney, K., Mei, F., Millller, M., Nascimento, R., Pauliquevis, T., Pekour, M., Peres, J., Petäjä, T.,

Pöhlklker, C., Pöschl, U., Rizzo, L., Schmid, B., Shilllling, J. E., Silva Dias, M. A., Smith, J. N., Tomlmlinson, J. M., Tóta, J., and Wendisch, M.: The green ocean amazon experiment (GOAMAZON2014/5) observes pollution affecting gases, aerosols, clouds, and rainfall over the rain forest, B. Am. Meteorol. Soc., 98, 981–997, https://doi.org/10.1175/BAMS-D-15-00221.1, 2017.

Moffet, R. C. and Prather, K. A.: In-situ measurements of the mixing state and optical properties of soot with implications for radiative forcing estimates, P. Natl. Acad. Sci. USA, 106, 11872–11877, https://doi.org/10.1073/pnas.0900040106, 2009.

Moran-Zuloaga, D., Ditas, F., Walter, D., Saturno, J., Brito, J., Carbone, S., Chi, X., Hrabě de Angelis, I., Baars, H., Godoi, R. H. M., Heese, B., Holanda, B. A., Lavrič, J. V., Martin, S. T., Ming, J., Pöhlker, M. L., Ruckteschler, N., Su, H., Wang, Y., Wang, Q., Wang, Z., Weber, B., Wolff, S., Artaxo, P., Pöschl, U., Andreae, M. O., and Pöhlker, C.: Long-term study on coarse mode aerosols in the Amazon rain forest with the frequent intrusion of Saharan dust plumes, Atmos. Chem. Phys., 18, 10055–10088, https://doi.org/10.5194/acp-18-10055-2018, 2018.

Olson, D. M., Dinerstein, E., Wikramanayake, E. D., Burgess, N. D., Powell, G. V. N., Underwood, E. C., D'amico, J. A., Itoua, I., Strand, H. E., Morrison, J. C., Loucks, C. J., Allnutt, T. F., Ricketts, T. H., Kura, Y., Lamoreux, J. F., Wettengel, W. W., Hedao, P., and Kassem, K. R.: Terrestrial Ecoregions of the World: A New Map of Life on Earth, Bioscience, 51, 933, https://doi.org/10.1641/0006-3568(2001)051[0933:teotwa]2.0.co;2, 2001.

Omar, A. H., Winker, D. M., Kittaka, C., Vaughan, M. A., Liu, Z., Hu, Y., Trepte, C. R., Rogers, R. R., Ferrare, R. A., Lee, K. P., Kuehn, R. E., and Hostetler, C. A.: The CALIPSO automated aerosol classification and lidar ratio selection algorithm, J. Atmos. Ocean. Tech., 26, 1994–2014, https://doi.org/10.1175/2009JTECHA1231.1, 2009.

Perry, K. D. and Hobbs, P. V.: Further evidence for particle nucleation in clear air adjacent to marine cumulus clouds, J. Geophys. Res., 99, 22803, https://doi.org/10.1029/94JD01926, 1994.

Pöhlker, C., Wiedemann, K. T., Sinha, B., Shiraiwa, M., Gunthe, S. S., Smith, M., Su, H., Artaxo, P., Chen, Q., Cheng, Y., Elbert, W., Gilles, M. K., Kilcoyne, A. L. D., Moffet, R. C., Weigand, M., Martin, S. T., Pöschl, U., and Andreae, M. O.: Biogenic Potassium Salt Particles as Seeds for Secondary Organic Aerosol in the Amazon, Science, 337, 1075–1078, https://doi.org/10.1126/science.1223264, 2012.

Pöhlker, C., Walter, D., Paulsen, H., Könemann, T., Rodríguez-Caballero, E., Moran-Zuloaga, D., Brito, J., Carbone, S., Degrendele, C., Després, V. R., Ditas, F., Holanda, B. A., Kaiser, J. W., Lammel, G., Lavrič, J. V., Ming, J., Pickersgill, D., Pöhlker, M. L., Praß, M., Löbs, N., Saturno, J., Sörgel, M., Wang, Q., Weber, B., Wolff, S., Artaxo, P., Pöschl, U., and Andreae, M. O.: Land cover and its transformation in the backward trajectory footprint region of the Amazon Tall Tower Observatory, Atmos. Chem. Phys., 19, 8425–8470, https://doi.org/10.5194/acp-19-8425-2019, 2019.

Pöhlker, M. L., Pöhlker, C., Ditas, F., Klimach, T., Hrabe de Angelis, I., Araújo, A., Brito, J., Carbone, S., Cheng, Y., Chi, X., Ditz, R., Gunthe, S. S., Kesselmeier, J., Könemann, T., Lavrič, J. V., Martin, S. T., Mikhailov, E., Moran-Zuloaga, D., Rose, D., Saturno, J., Su, H., Thalman, R., Walter, D., Wang, J., Wolff, S., Barbosa, H. M. J., Artaxo, P., Andreae, M. O., and Pöschl, U.: Long-term observations of cloud condensation nuclei in the Amazon rain forest – Part 1: Aerosol size distribution, hygroscopicity, and new model parametrizations for CCN prediction, Atmos. Chem. Phys., 16, 15709–15740, https://doi.org/10.5194/acp-16-15709-2016, 2016.

Pöhlker, M. L., Ditas, F., Saturno, J., Klimach, T., Hrabě de Angelis, I., Araùjo, A. C., Brito, J., Carbone, S., Cheng, Y., Chi, X., Ditz, R., Gunthe, S. S., Holanda, B. A., Kandler, K., Kesselmeier, J., Könemann, T., Krüger, O. O., Lavrič, J. V., Martin, S. T., Mikhailov, E., Moran-Zuloaga, D., Rizzo, L. V., Rose, D., Su, H., Thalman, R., Walter, D., Wang, J., Wolff, S., Barbosa, H. M. J., Artaxo, P., Andreae, M. O., Pöschl, U., and Pöhlker, C.: Long-term observations of cloud condensation nuclei over the Amazon rain forest – Part 2: Variability and characteristics of biomass burning, long-range transport, and pristine rain forest aerosols, Atmos. Chem. Phys., 18, 10289–10331, https://doi.org/10.5194/acp-18-10289-2018, 2018.

Pokhrel, R. P., Beamesderfer, E. R., Wagner, N. L., Langridge, J. M., Lack, D. A., Jayarathne, T., Stone, E. A., Stockwell, C. E., Yokelson, R. J., and Murphy, S. M.: Relative importance of black carbon, brown carbon, and absorption enhancement from clear coatings in biomass burning emissions, Atmos. Chem. Phys., 17, 5063–5078, https://doi.org/10.5194/acp-17-5063-2017, 2017.

Pöschl, U., Martin, S. T., Sinha, B., Chen, Q., Gunthe, S. S., Huffman, J. A., Borrmann, S., Farmer, D. K., Garland, R. M., Helas, G., Jimenez, J. L., King, S. M., Manzi, A., Mikhailov, E., Pauliquevis, T., Petters, M. D., Prenni, A. J., Roldin, P., Rose, D., Schneider, J., Su, H., Zorn, S. R., Artaxo, P., and Andreae, M. O.: Rainforest Aerosols as Biogenic Nuclei of Clouds and Precipitation in the Amazon, Science, 329, 1513–1516, https://doi.org/10.1126/science.1191056, 2010.

Reddington, C. L., Spracklen, D. V., Artaxo, P., Ridley, D. A., Rizzo, L. V., and Arana, A.: Analysis of particulate emissions from tropical biomass burning using a global aerosol model and long-term surface observations, Atmos. Chem. Phys., 16, 11083–11106, https://doi.org/10.5194/acp-16-11083-2016, 2016.

Reid, J. S., Koppmann, R., Eck, T. F., and Eleuterio, D. P.: A review of biomass burning emissions part II: intensive physical properties of biomass burning particles, Atmos. Chem. Phys., 5, 799–825, https://doi.org/10.5194/acp-5-799-2005, 2005.

Remer, L. A., Kaufman, Y. J., Tanré, D., Mattoo, S., Chu, D. A., Martins, J. V., Li, R.-R., Ichoku, C., Levy, R. C., Kleidman, R. G., Eck, T. F., Vermote, E., and Holben, B. N.: The MODIS Aerosol Algorithm, Products, and Validation, J. Atmos. Sci., 62, 947–973, https://doi.org/10.1175/JAS3385.1, 2005.

Rizzo, L. V., Artaxo, P., Müller, T., Wiedensohler, A., Paixão, M., Cirino, G. G., Arana, A., Swietlicki, E., Roldin, P., Fors, E. O., Wiedemann, K. T., Leal, L. S. M., and Kulmala, M.: Long term measurements of aerosol optical properties at a primary forest site in Amazonia, Atmos. Chem. Phys., 13, 2391–2413, https://doi.org/10.5194/acp-13-2391-2013, 2013.

Roberts, G. C.: Impact of biomass burning on cloud properties in the Amazon Basin, J. Geophys. Res., 108, 4062, https://doi.org/10.1029/2001JD000985, 2003.

Roberts, G. C. and Nenes, A.: A continuous-flow streamwise thermal-gradient CCN chamber for atmospheric measurements, Aerosol Sci. Tech., 39, 206–221, https://doi.org/10.1080/027868290913988, 2005.

Roberts, G. C., Andreae, M. O., Zhou, J., and Artaxo, P.: Cloud condensation nuclei in the Amazon Basin: "marine" conditions over a continent?, Geophys. Res. Lett., 28, 2807–2810, https://doi.org/10.1029/2000GL012585, 2001.

Rose, D., Gunthe, S. S., Mikhailov, E., Frank, G. P., Dusek, U., Andreae, M. O., and Pöschl, U.: Calibration and measurement uncertainties of a continuous-flow cloud condensation nuclei counter (DMT-CCNC): CCN activation of ammonium sulfate and sodium chloride aerosol particles in theory and experiment, Atmos. Chem. Phys., 8, 1153–1179, https://doi.org/10.5194/acp-8-1153-2008, 2008.

Saturno, J., Ditas, F., Penning de Vries, M., Holanda, B. A., Pöhlker, M. L., Carbone, S., Walter, D., Bobrowski, N., Brito, J., Chi, X., Gutmann, A., Hrabe de Angelis, I., Machado, L. A. T., Moran-Zuloaga, D., Rüdiger, J., Schneider, J., Schulz, C., Wang, Q., Wendisch, M., Artaxo, P., Wagner, T., Pöschl, U., Andreae, M. O., and Pöhlker, C.: African volcanic emissions influencing atmospheric aerosols over the Amazon rain forest, Atmos. Chem. Phys., 18, 10391–10405, https://doi.org/10.5194/acp-18-10391-2018, 2018a.

Saturno, J., Holanda, B. A., Pöhlker, C., Ditas, F., Wang, Q., Moran-Zuloaga, D., Brito, J., Carbone, S., Cheng, Y., Chi, X., Ditas, J., Hoffmann, T., Hrabe de Angelis, I., Könemann, T., Lavrič, J. V., Ma, N., Ming, J., Paulsen, H., Pöhlker, M. L., Rizzo, L. V., Schlag, P., Su, H., Walter, D., Wolff, S., Zhang, Y., Artaxo, P., Pöschl, U., and Andreae, M. O.: Black and brown carbon over central Amazonia: long-term aerosol measurements at the ATTO site, Atmos. Chem. Phys., 18, 12817–12843, https://doi.org/10.5194/acp-18-12817-2018, 2018b.

Schill, G. P., Froyd, K. D., Bian, H., Brock, C. B., Ray, E., Hornbrook, R. S., Hills, A. J., Apel, E. C., Chen, M., Colarco, P., and Murphy, D. M.: The ubiquity of dilute, aged smoke in the global remote troposphere and its effect on climate, Nat. Geosci., in preparation, 2019.

Schnaiter, M.: Absorption amplification of black carbon internally mixed with secondary organic aerosol, J. Geophys. Res., 110, D19204, https://doi.org/10.1029/2005JD006046, 2005.

Schneider, J., Freutel, F., Zorn, S. R., Chen, Q., Farmer, D. K., Jimenez, J. L., Martin, S. T., Artaxo, P., Wiedensohler, A., and Borrmann, S.: Mass-spectrometric identification of primary biological particle markers and application to pristine submicron aerosol measurements in Amazonia, Atmos. Chem. Phys., 11, 11415–11429, https://doi.org/10.5194/acp-11-11415-2011, 2011.

Schulz, C., Schneider, J., Amorim Holanda, B., Appel, O., Costa, A., de Sá, S. S., Dreiling, V., Fütterer, D., Jurkat-Witschas, T., Klimach, T., Knote, C., Krämer, M., Martin, S. T., Mertes, S., Pöhlker, M. L., Sauer, D., Voigt, C., Walser, A., Weinzierl, B., Ziereis, H., Zöger, M., Andreae, M. O., Artaxo, P., Machado, L. A. T., Pöschl, U., Wendisch, M., and Borrmann, S.: Aircraft-based observations of isoprene-epoxydiol-derived secondary organic aerosol (IEPOX-SOA) in the tropical upper troposphere over the Amazon region, Atmos. Chem. Phys., 18, 14979–15001, https://doi.org/10.5194/acp-18-14979-2018, 2018.

Schwarz, J. P., Gao, R. S., Fahey, D. W., Thomson, D. S., Watts, L. A., Wilson, J. C., Reeves, J. M., Darbeheshti, M., Baumgardner, D. G., Kok, G. L., Chung, S. H., Schulz, M., Hendricks, J., Lauer, A., Kärcher, B., Slowik, J. G., Rosenlof, K. H., Thompson, T. L., Langford, A. O., Loewenstein, M., and Aikin, K. C.: Single-particle measurements of midlatitude black carbon and light-scattering aerosols from the boundary layer to the lower stratosphere, J. Geophys. Res.-Atmos., 111, 1–15, https://doi.org/10.1029/2006JD007076, 2006.

Schwarz, J. P., Gao, R. S., Spackman, J. R., Watts, L. A., Thomson, D. S., Fahey, D. W., Ryerson, T. B., Peischl, J., Holloway, J. S., Trainer, M., Frost, G. J., Baynard, T., Lack, D. A., de Gouw, J. A., Warneke, C., and Del Negro, L. A.: Measurement of the mixing state, mass, and optical size of individual black carbon particles in urban and biomass burning emissions, Geophys. Res. Lett., 35, 1–5, https://doi.org/10.1029/2008GL033968, 2008.

Shrivastava, M., Andreae, M. O., Artaxo, P., Barbosa, H. M. J., Berg, L. K., Brito, J., Ching, J., Easter, R. C., Fan, J., Fast, J. D., Feng, Z., Fuentes, J. D., Glasius, M., Goldstein, A. H., Alves, E. G., Gomes, H., Gu, D., Guenther, A., Jathar, S. H., Kim, S., Liu, Y., Lou, S., Martin, S. T., McNeill, V. F., Medeiros, A., de Sá, S. S., Shilling, J. E., Springston, S. R., Souza, R. A. F., Thornton, J. A., Isaacman-VanWertz, G., Yee, L. D., Ynoue, R., Zaveri, R. A., Zelenyuk, A., and Zhao, C.: Urban pollution greatly enhances formation of natural aerosols over the Amazon rainforest, Nat. Commun., 10, 1046, https://doi.org/10.1038/s41467-019-08909-4, 2019.

Slowik, J. G., Wong, J. P. S., and Abbatt, J. P. D.: Real-time, controlled OH-initiated oxidation of biogenic secondary organic aerosol, Atmos. Chem. Phys., 12, 9775–9790, https://doi.org/10.5194/acp-12-9775-2012, 2012.

Stamnes, K., Tsay, S.-C., Wiscombe, W., and Laszlo, I.: DISORT, A General-Purpose Fortran Program for Discrete Ordinate-Method Radiative Transfer in Scattering and Emitting Layered Media: Documentation of Methodology, Tech. rep., Dept. of Physics and Engineering Physics, Stevens Institute of Technology, Hoboken, NJ 07030, 2000.

Stein, A. F., Draxler, R. R., Rolph, G. D., Stunder, B. J. B., Cohen, M. D., and Ngan, F.: NOAA's HYSPLIT Atmospheric Transport and Dispersion Modeling System, B. Am. Meteorol. Soc., 96, 2059–2077, https://doi.org/10.1175/BAMS-D-14-00110.1, 2015.

Stephens, M., Turner, N., and Sandberg, J.: Particle identification by laser-induced incandescence in a solid-state laser cavity, Appl. Optics, 42, 3726–36, https://doi.org/10.1364/AO.42.003726, 2003.

Swap, R., Garstang, M., Greco, S., Talbot, R., and Kallberg, P.: Saharan dust in the Amazon Basin, Tellus B, 44, 133–149, https://doi.org/10.1034/j.1600-0889.1992.t01-1-00005.x, 1992.

Talbot, R. W., Andreae, M. O., Berresheim, H., Artaxo, P., Garstang, M., Harriss, M., Beecher, K. M., and Li, S.-M.: Aerosol Chemistry During the Wet Season in Central Amazonia?: The Influence of Long-Range Transport, J. Geophys. Res., 95, 16955–16969, 1990.

Thompson, A. M., Diab, R. D., Bodeker, G. E., Zunckel, M., Coetzee, G. J. R., Archer, C. B., McNamara, D. P., Pickering, K. E., Combrink, J., Fishman, J., and Nganga, D.: Ozone over southern Africa during SAFARI-92/TRACE A, J. Geophys. Res.-Atmos., 101, 23793–23807, https://doi.org/10.1029/95JD02459, 1996.

Tritscher, T., Jurányi, Z., Martin, M., Chirico, R., Gysel, M., Heringa, M. F., DeCarlo, P. F., Sierau, B., Prévôt, A. S. H., Weingartner, E., and Baltensperger, U.: Changes of hygroscopicity and morphology during ageing of diesel soot, Environ. Res. Lett., 6, 034026, https://doi.org/10.1088/1748-9326/6/3/034026, 2011.

Wang, Q., Saturno, J., Chi, X., Walter, D., Lavric, J. V., Moran-Zuloaga, D., Ditas, F., Pöhlker, C., Brito, J., Carbone, S., Artaxo, P., and Andreae, M. O.: Modeling investigation of light-absorbing aerosols in the Amazon Basin during the wet season, Atmos. Chem. Phys., 16, 14775–14794, https://doi.org/10.5194/acp-16-14775-2016, 2016.

Weinzierl, B., Sauer, D., Esselborn, M., Petzold, A., Veira, A., Rose, M., Mund, S., Wirth, M., Ansmann, A., Tesche, M., Gross, S., and Freudenthaler, V.: Microphysical and optical properties of dust and tropical biomass burning aerosol layers in the Cape Verde region-an overview of the airborne in situ and lidar measurements during SAMUM-2, Tellus B, 63, 589–618, https://doi.org/10.1111/j.1600-0889.2011.00566.x, 2011.

Wendisch, M., Pöschl, U., Andreae, M. O., MacHado, L. A. T., Albrecht, R., Schlager, H., Rosenfeld, D., Martin, S. T., Abdelmonem, A., Afchine, A., Araujo, A. C., Artaxo, P., Aufmhoff, H., Barbosa, H. M. J., Borrmann, S., Braga, R., Buchholz, B., Cecchini, M. A., Costa, A., Curtius, J., Dollner, M., Dorf, M., Dreiling, V., Ebert, V., Ehrlich, A., Ewald, F., Fisch, G., Fix, A., Frank, F., Futterer, D., Heckl, C., Heidelberg, F., Huneke, T., Jakel, E., Jarvinen, E., Jurkat, T., Kanter, S., Kastner, U., Kenntner, M., Kesselmeier, J., Klimach, T., Knecht, M., Kohl, R., Kolling, T., Kramer, M., Kruger, M., Krisna, T. C., Lavric, J. V., Longo, K., Mahnke, C., Manzi, A. O., Mayer, B., Mertes, S., Minikin, A., Molleker, S., Munch, S., Nillius, B., Pfeilsticker, K., Pohlker, C., Roiger, A., Rose, D., Rosenow, D., Sauer, D., Schnaiter, M., Schneider, J., Schulz, C., De Souza, R. A. F., Spanu, A., Stock, P., Vila, D., Voigt, C., Walser, A., Walter, D., Weigel, R., Weinzierl, B., Werner, F., Yamasoe, M. A., Ziereis, H., Zinner, T., and Zoger, M.: Acridicon-chuva campaign: Studying tropical deep convective clouds and precipitation over amazonia using the New German research aircraft HALO, B. Am. Meteorol. Soc., 97, 1885–1908, https://doi.org/10.1175/BAMS-D-14-00255.1, 2016.

van der Werf, G. R., Randerson, J. T., Giglio, L., van Leeuwen, T. T., Chen, Y., Rogers, B. M., Mu, M., van Marle, M. J. E., Morton, D. C., Collatz, G. J., Yokelson, R. J., and Kasibhatla, P. S.: Global fire emissions estimates during 1997–2016, Earth Syst. Sci. Data, 9, 697–720, https://doi.org/10.5194/essd-9-697-2017, 2017.

Willis, M. D., Healy, R. M., Riemer, N., West, M., Wang, J. M., Jeong, C.-H., Wenger, J. C., Evans, G. J., Abbatt, J. P. D., and Lee, A. K. Y.: Quantification of black carbon mixing state from traffic: implications for aerosol optical properties, Atmos. Chem. Phys., 16, 4693–4706, https://doi.org/10.5194/acp-16-4693-2016, 2016.

Winderlich, J., Chen, H., Gerbig, C., Seifert, T., Kolle, O., Lavrič, J. V., Kaiser, C., Höfer, A., and Heimann, M.: Continuous low-maintenance $CO_2/CH_4/H_2O$ measurements at the Zotino Tall Tower Observatory (ZOTTO) in Central Siberia, Atmos. Meas. Tech., 3, 1113–1128, https://doi.org/10.5194/amt-3-1113-2010, 2010.

Winker, D. M., Vaughan, M. A., Omar, A., Hu, Y., Powell, K. A., Liu, Z., Hunt, W. H., and Young, S. A.: Overview of the CALIPSO Mission and CALIOP Data Processing Algorithms, J. Atmos. Ocean. Tech., 26, 2310–2323, https://doi.org/10.1175/2009JTECHA1281.1, 2009.

Wong, J. P. S., Tsagkaraki, M., Tsiodra, I., Mihalopoulos, N., Violaki, K., Kanakidou, M., Sciare, J., Nenes, A., and Weber, R. J.: Atmospheric evolution of molecular-weight-separated brown carbon from biomass burning, Atmos. Chem. Phys., 19, 7319–7334, https://doi.org/10.5194/acp-19-7319-2019, 2019.

Wu, H., Taylor, J. W., Szpek, K., Langridge, J., Williams, P. I., Flynn, M., Allan, J. D., Abel, S. J., Pitt, J., Cotterell, M. I., Fox, C., Davies, N. W., Haywood, J., and Coe, H.: Vertical variability of the properties of highly aged biomass burning aerosol transported over the southeast Atlantic during CLARIFY-2017, Atmos. Chem. Phys. Discuss., https://doi.org/10.5194/acp-2020-197, in review, 2020.

Yasunari, T. J., Koster, R. D., Lau, K. M., Aoki, T., Sud, Y. C., Yamazaki, T., Motoyoshi, H., and Kodama, Y.: Influence of dust and black carbon on the snow albedo in the NASA Goddard Earth Observing System version 5 land surface model, J. Geophys. Res.-Atmos., 116, D02210, https://doi.org/10.1029/2010JD014861, 2011.

Zhang, J., Liu, J., Tao, S., and Ban-Weiss, G. A.: Long-range transport of black carbon to the Pacific Ocean and its dependence on aging timescale, Atmos. Chem. Phys., 15, 11521–11535, https://doi.org/10.5194/acp-15-11521-2015, 2015.

Zhou, S., Collier, S., Jaffe, D. A., Briggs, N. L., Hee, J., Sedlacek III, A. J., Kleinman, L., Onasch, T. B., and Zhang, Q.: Regional influence of wildfires on aerosol chemistry in the western US and insights into atmospheric aging of biomass burning organic aerosol, Atmos. Chem. Phys., 17, 2477–2493, https://doi.org/10.5194/acp-17-2477-2017, 2017.

Ziereis, H., Schlager, H., Schulte, P., van Velthoven, P. F. J., and Slemr, F.: Distributions of NO, NO_x, and NO_y in the upper troposphere and lower stratosphere between 28° and 61° N during POLINAT 2, J. Geophys. Res.-Atmos., 105, 3653–3664, https://doi.org/10.1029/1999JD900870, 2000.

Zuidema, P., Redemann, J., Haywood, J., Wood, R., Piketh, S., Hipondoka, M., and Formenti, P.: Smoke and Clouds above the Southeast Atlantic: Upcoming Field Campaigns Probe Absorbing Aerosol's Impact on Climate, B. Am. Meteorol. Soc., 97, 1131–1135, https://doi.org/10.1175/BAMS-D-15-00082.1, 2016.

Zuidema, P., Sedlacek, A. J., Flynn, C., Springston, S., Delgadillo, R., Zhang, J., Aiken, A. C., Koontz, A., and Muradyan, P.: The Ascension Island Boundary Layer in the Remote Southeast Atlantic is Often Smoky, Geophys. Res. Lett., 45, 4456–4465, https://doi.org/10.1002/2017GL076926, 2018.